

This is the accepted manuscript made available via CHORUS. The article has been published as:

Effect of atomic disorder and Ce doping on
superconductivity of $\text{Ca}_{\{3\}}\text{Rh}_{\{4\}}\text{Sn}_{\{13\}}$: Electric
transport properties under high pressure

A. Ślebarski, J. Goraus, M. M. Mańska, P. Witas, M. Fijałkowski, C. T. Wolowiec, Y. Fang, and
M. B. Maple

Phys. Rev. B **93**, 245126 — Published 13 June 2016

DOI: [10.1103/PhysRevB.93.245126](https://doi.org/10.1103/PhysRevB.93.245126)

Effect of atomic disorder and Ce doping on superconductivity of $\text{Ca}_3\text{Rh}_4\text{Sn}_{13}$; electric transport properties under high pressure.

A. Ślebarski^{1,2}, J. Goraus¹, M. M. Maška¹, P. Witas¹, M. Fijałkowski¹, C. T. Wolowiec³, Y. Fang^{3,4}, and M. B. Maple³

¹*Institute of Physics, University of Silesia, Uniwersytecka 4, 40-007 Katowice, Poland*

²*Centre for Advanced Materials and Smart Structures,*

Polish Academy of Sciences, Okólna 2, 50-950 Wrocław, Poland

³*Department of Physics, University of California, San Diego, La Jolla, California 92093, USA*

⁴*Materials Science and Engineering Program, University of California, San Diego, La Jolla, California 92093, USA*

We report the observation of a superconducting state below ~ 8 K coexistent with a spin-glass state caused by atomic disorder in Ce substituted $\text{Ca}_3\text{Rh}_4\text{Sn}_{13}$. Measurements of specific heat, resistivity, and magnetism reveal the existence of inhomogeneous superconductivity in samples doped with Ce with superconducting critical temperatures T_c higher than those observed in the parent compound. For $\text{Ca}_3\text{Rh}_4\text{Sn}_{13}$, the negative value of the change in resistivity ρ with pressure P , $\frac{d\rho}{dP}$ correlates well with the calculated decrease in the density of states (DOS) at the Fermi energy with P . Based on band structure calculations performed under pressure, we demonstrate how the change in DOS would affect T_c of $\text{Ca}_3\text{Rh}_4\text{Sn}_{13}$ under negative lattice pressure in samples that are strongly defected by quenching.

PACS numbers: 71.27.+a, 72.15.Qm, 71.20.-b, 72.15.-v

I. INTRODUCTION

The interplay of magnetic order and superconductivity is a key topic of current research of strongly correlated heavy fermion compounds, high- T_c cuprates as well as iron-based pnictide or chalcogenide superconductors. The destruction of superconductivity at the onset of magnetic order has been well known; however, there are an increasing number of new superconductors which are found experimentally to be closely linked to magnetism. Analysis of the magnetic ordering and its coexistence with superconductivity may help to explain the pairing mechanism in high- T_c and unconventional superconductors. In particular, very recent reports demonstrate coexistence of superconducting and spin-glass-like states in $\text{EuFe}_2(\text{As}_{1-x}\text{P}_x)_2$ ¹, and $\text{Ca}_{0.9}\text{Ce}_{0.1}\text{Fe}_2\text{As}_2$ ², which suggests an important role of atomic disorder.

There are a number of strongly correlated superconductors including $\text{Bi}_2\text{Sr}_2\text{CaCu}_2\text{O}_{8+x}$, $\text{PrOs}_4\text{Sb}_{12}$ ^{3,4}, CePt_3Si ^{5,6}, and CeIrIn_5 ⁷, in which the nanoscale electronic disorder is responsible for an increase in T_c . Similar behavior has been found in $\text{La}_3\text{Rh}_4\text{Sn}_{13}$ ⁸ and $\text{La}_3\text{Ru}_4\text{Sn}_{13}$ ⁹, where nanoscale electronic disorder leads to the increase of T_c . Regarding the filamentary superconductivity observed in known granular superconductors, it has been reported¹⁰, for example, that the filamentary superconductivity in CaFe_2As_2 suggests that even nominally pure stoichiometric compounds can spontaneously become electronically inhomogeneous at the nanoscale. In the similar compound, BaFe_2As_2 ,¹¹ a spin-glass-like antiferromagnetic state was found to be coexist with superconductivity along domain walls. It is widely believed that disorder plays a key role in the new superconductors. In particular, such disorder can have noticeable effects on T_c . In this study, we report an increase in T_c when Ce is substituted for Ca in the skutterudite-related $\text{Ca}_3\text{Rh}_4\text{Sn}_{13}$ superconductor. We argue that it

can be a result of the disorder induced by the substitution. The results will contribute to a better understanding of the complex low temperature properties observed in novel superconducting strongly correlated electron systems.

II. EXPERIMENTAL DETAILS

The $\text{Ca}_3\text{Rh}_4\text{Sn}_{13}$ and $\text{Ce}_x\text{Rh}_4\text{Sn}_{13}$ polycrystalline samples were prepared by arc melting the constituent elements on a water cooled copper hearth in a high-purity argon atmosphere with an Al getter. The $\text{Ca}_{3-x}\text{Ce}_x\text{Rh}_4\text{Sn}_{13}$ alloys were then prepared by diluting the parent compounds with nominal compositions of Ce and Ca which were then annealed at 870°C for 2 weeks. All samples were examined by x-ray diffraction (XRD) analysis and found to have a cubic structure (space group $\text{Pm}\bar{3}\text{n}$)¹². XRD data were refined using FULPROF program¹³ with pseudo-Voigt line shape, yielding the profile R -factor $R_p < 4$, the weighted profile R -factor $R_{wp} < 5$, and $R_{exp} \approx 0.5$. Figure 1a shows a representative XRD pattern for $\text{Ca}_3\text{Rh}_4\text{Sn}_{13}$ together with its Rietveld refined pattern. From the XRD patterns measured at $T = 300$ K, 160 K and 12 K we identified the cubic structure of $\text{Yb}_3\text{Rh}_4\text{Sn}_{13}$ -type for $\text{Ca}_3\text{Rh}_4\text{Sn}_{13}$. No evidence of simple cubic-to-bcc structural distortion was found in $\text{Ca}_3\text{Rh}_4\text{Sn}_{13}$, while the low-temperature XRD data show superlattice reflections for $x \geq 1.5$ components of $\text{Ca}_{3-x}\text{Ce}_x\text{Rh}_4\text{Sn}_{13}$ in the low 2θ region (see Fig. 2a), interpreted (c.f. Refs.^{14,15}) as a structural transition from simple cubic to $\text{I}\bar{4}3\text{d}$ bcc structure, involving crystallographic cell doubling. Fig. 2b exhibits the abnormal volume change at the temperature of structural distortion found for $x \geq 1.5$, which is, however, not observed for the parent compound. The refined lattice parameters shown in Fig. 1c and corresponding atomic positions

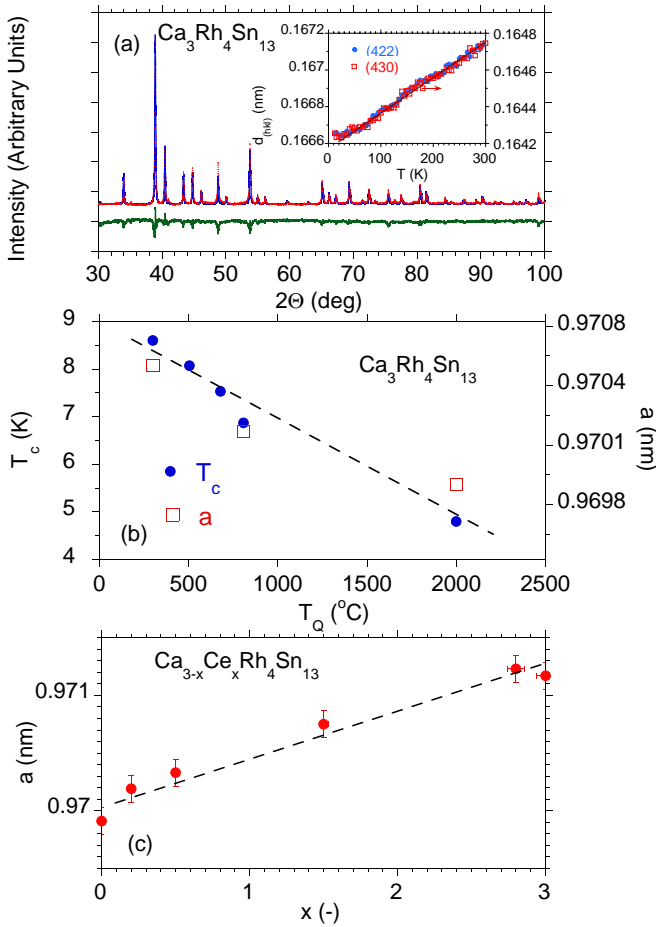


FIG. 1. (a) X-ray diffraction pattern for the $\text{Ca}_3\text{Rh}_4\text{Sn}_{13}$ compound. The green line represents the differences between the blue and red line peak shapes. Inset: The temperature change of the (422) and (430) XRD lines between 12 K and 300 K. There was no change of d_{hkl} vs T , characteristic of the structural phase transition. (b) T_c and the lattice parameter a for $\text{Ca}_3\text{Rh}_4\text{Sn}_{13}$ plotted against different quenching temperatures T_Q . The data at $T_Q = 505, 679,$ and 804°C are taken from Ref. 17. Temperature $T_c = 4.8$ K and the room temperature lattice parameter $a = 9.6991$ Å for the arc-melted sample are expected at $T_Q \sim 2000$ K. (c) The lattice parameter, a , plotted against Ce concentration, x , for the $\text{Ca}_{3-x}\text{Ce}_x\text{Rh}_4\text{Sn}_{13}$ system. The dotted line is a linear fit to the data.

were used in our band structure calculations. The lattice parameters of the $\text{Ca}_{3-x}\text{Ce}_x\text{Rh}_4\text{Sn}_{13}$ alloys measured at room temperature follow Vegard's law, which suggests good sample quality and stoichiometry of the components x . Stoichiometry and homogeneity were checked by the electron microprobe technique (scanning microscope JSM-5410) and by XPS analysis. Deviations from the nominal composition were small. The experimentally obtained compositions from the total surface of the sample were very close to the assumed one; e.g., for $\text{Ca}_{2.6}\text{Ce}_{0.6}\text{Rh}_4\text{Sn}_{13}$ with the assumed atomic concentration ratio 12:3:20:65, respectively we determined 12.05 at.% Ca, 3.04 at.% Ce, 19.60 at.% Rh, and 65.31 at.%

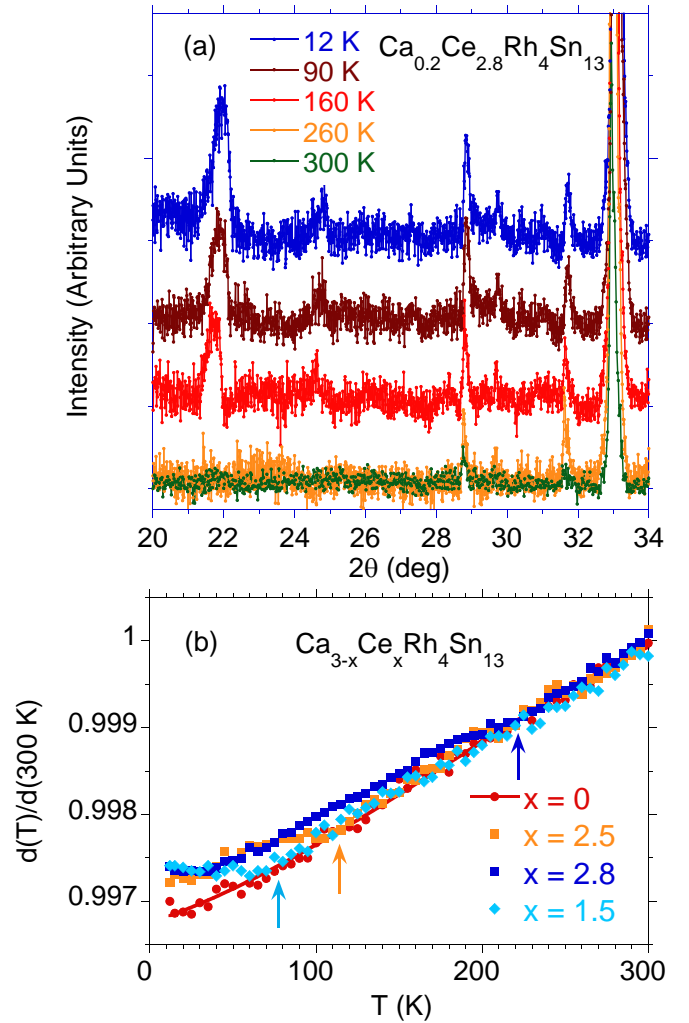


FIG. 2. (a) X-ray diffraction of $\text{Ca}_{0.2}\text{Ce}_{2.8}\text{Rh}_4\text{Sn}_{13}$ with $\text{Cu } K_\alpha$ radiation at different temperatures for small 2θ s to exhibit additional superlattice reflections at $T = 160$ K and below. (b) The temperature change of the distance $d(T)$ in different compounds $\text{Ca}_{1-x}\text{Ce}_x\text{Rh}_4\text{Sn}_{13}$, normalized to the d value at $T = 300$ K between (422) crystallographic planes, obtained from Bragg equation $\lambda = 2d \sin \theta(T)$ for diffraction line (422). Arrows indicate the temperature of the structural distortion (T_D) for the components $x = 1.5, 2.5,$ and 2.8 . There is a change of intensity of the XRD diffraction lines at T_D , not shown here (c.f. Ref. 16). In panel (a), for $T \leq 160$ K the intensity of the superlattice reflection at $2\theta \approx 22$ deg shows linear increase vs decreasing T .

Sn. The variations in stoichiometry over the length of the sample are shown for this sample in Fig. 3. Local fluctuations in composition were observed in nano-scale for all components of the alloy, however, the greatest one exist for Ce, which may explain the strong disorder induced by doping. We observed similar fluctuations in the composition for the parent compound, which signals similar site disorder induced by rapid quenching from high temperature in the system of $\text{Ca}_{3-x}\text{Ce}_x\text{Rh}_4\text{Sn}_{13}$ alloys.

The difference spectrum shown in Fig. 1a (green

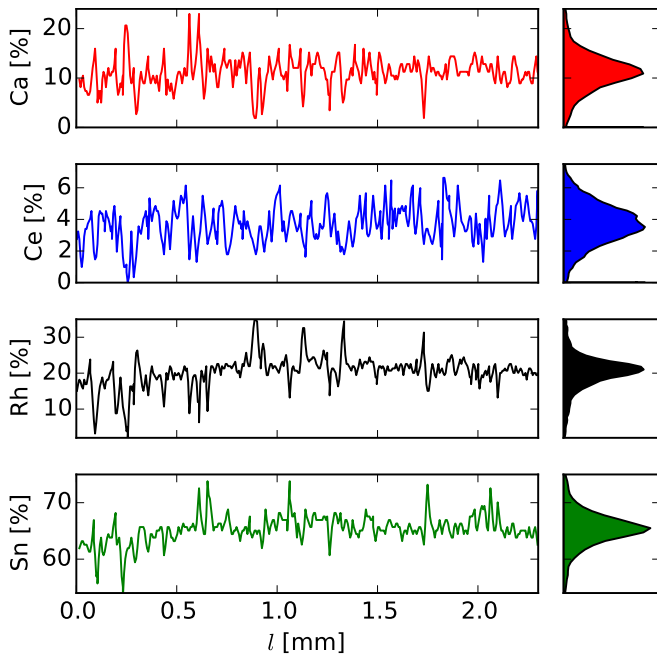


FIG. 3. Variations in stoichiometry of $\text{Ca}_{2.4}\text{Ce}_{0.6}\text{Rh}_4\text{Sn}_{13}$ over the length of the sample. The right panels show corresponding histograms.

line) results from the differences in peak shape, which we attribute to atomic disorder in $\text{Ca}_3\text{Rh}_4\text{Sn}_{13}$. It was reported^{17,18}, that Ca-Sn1 anti-site defects generated at high temperatures and then frozen-in by rapid quenching to room temperature are responsible either for the degradation of the superconducting transition temperature T_c or a reduction in the lattice parameter a in $\text{Ca}_3\text{Rh}_4\text{Sn}_{13}$. Figure 1b exhibits the T_c vs T_Q (the temperature from which the samples were quenched) data taken from Ref. 17. In the quenching temperature range $\sim 810 - 300$ °C, T_c of $\text{Ca}_3\text{Rh}_4\text{Sn}_{13}$ is lowered from 8.4 K in the as-grown sample down to 6.9 K in the sample which was quenched at ~ 810 K¹⁷. Hence, the value of $T_c \sim 4.8$ K and the lattice parameter $a = 9.6991$ Å for the sample melted in arc (shown in the figure) can be explained by rapid quenching at T_Q of about 2000–3000 K.

Electrical resistivity ρ at ambient pressure was investigated by a conventional four-point ac technique using a Quantum Design Physical Properties Measurement System (PPMS). Measurements of ρ under pressure were performed in a beryllium-copper, piston-cylinder clamped cell (for details, see Ref. 19).

Specific heat C was measured in the temperature range 0.4–300 K and in external magnetic fields up to 9 T using a Quantum Design PPMS platform. The dc magnetization M and (dc and ac) magnetic susceptibility χ were obtained using a commercial superconducting quantum interference device magnetometer from 1.8 K to 300 K in magnetic fields up to 7 T.

The XPS spectra were obtained with monochroma-

tized Al K_α radiation at room temperature using a PHI 5700 ESCA spectrometer. The polycrystalline sample was broken under high vacuum better than 6×10^{-10} Torr immediately before taking a spectrum.

The band structure calculations were accomplished using fully relativistic full potential local orbital method (FPLO9-00-34 computer code²⁰) within the local spin density approximation (LSDA) as well as ELK FP-LAPW/APW+lo code²¹. The exchange correlation potential V_{xc} was used in the form proposed by Perdew-Wang²² in both cases. The number of k-points in the irreducible wedge of Brillouin Zone was 80. The results obtained from both methods were accomplished for the same V_{xc} , and as expected were essentially the same. The ELK-code was used for accurate calculations of the electron localization function (ELF), whereas the FPLO method was used to study the pressure influence as it is much faster due to a more advanced mixing scheme.

III. RESULTS AND DISCUSSION

A. Atomic disorder and superconductivity in $\text{Ca}_3\text{Rh}_4\text{Sn}_{13}$ revisited

1. Magnetic properties of $\text{Ca}_3\text{Rh}_4\text{Sn}_{13}$ doped with Ce, evidence of short range magnetic order and the superconducting state

$\text{Ca}_3\text{Rh}_4\text{Sn}_{13}$ has been reported to be a paramagnetic²³ superconducting compound with a $T_c \sim 8.4$ K. However, the superconducting state of this compound was proposed¹⁷ to be strongly dependent on the atomic disorder, which, upon quenching, leads to a significant decrease in T_c . On the other hand, there are some examples of analogous skutterudite-related superconductors ($\text{La}_3\text{Rh}_4\text{Sn}_{13}$ ²⁴, $\text{La}_3\text{Ru}_4\text{Sn}_{13}$ ⁹) which show evidence of nanoscale disorder over length scales similar to the coherence length as a bulk property, leading to an inhomogeneous superconducting state with an enhanced critical temperature $T_c^* > T_c$. Here, T_c^* represents a drop of resistivity connected to formation of percolation paths, whereas T_c , determined from the specific heat, indicates the onset of bulk superconductivity. This behavior is also observed in other strongly correlated f -electron superconductors which we believe will attract future attention. With this motivation, we present the magnetic investigations of $\text{Ca}_3\text{Rh}_4\text{Sn}_{13}$ substituted with Ce. The χ vs T dc magnetic susceptibility data obtained at 500 Oe in zero field (ZFC) and field cooling (FC) modes shown in Fig. 4 reveals the onset of diamagnetism and thermal hysteresis associated with the superconducting state below $T_c \approx 4.8$ K for $\text{Ca}_3\text{Rh}_4\text{Sn}_{13}$. At the concentration of Ce $x = 0.1$ T_c jumps to about 8 K and remains at this value for x up to 1. Then, with further increase of x it drops down and at $x = 1.5$ there is no superconductivity. For a wide range of Ce concentrations two superconducting transitions are observed, what will be discussed later.

Fig. 5 shows how these temperatures depend on x . Since the critical temperature first increases with increasing x , then reaches maximum at *optimal doping* and then decreases, it forms a *dome* similar to that which is typical for the *high* - T_c cuprates. Of course, the main difference is that for $\text{Ca}_3\text{Rh}_4\text{Sn}_{13}$ doped with Ce, there is no lower critical concentration of Ce and as such the undoped parent compound $\text{Ca}_3\text{Rh}_4\text{Sn}_{13}$ is superconducting. Within the *superconducting dome* there are two effects of disorder on the superconductivity, namely the site disorder induced by rapid quenching from high temperature which decreases T_c in the parent compound and the disorder that results from doping with cerium, which increases superconducting transition. The effect of these two types of disorder is clearly seen in Fig. 5; these two types of disorder roughly can be distinguished by microanalysis (c.f. Fig. 3 and comment). Measure-

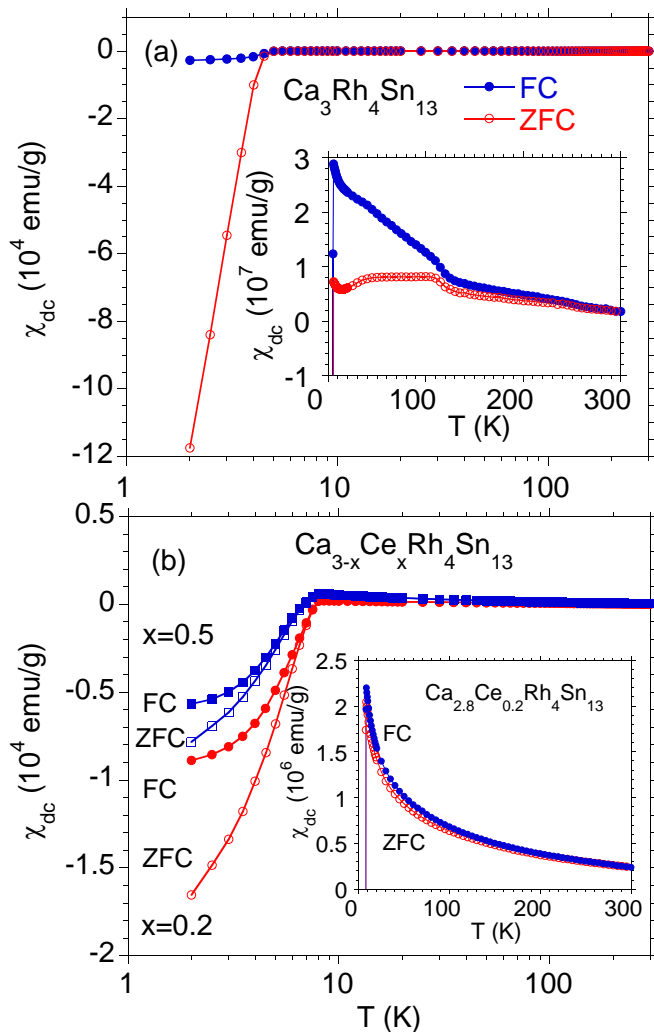


FIG. 4. Magnetic susceptibility (dc) for $\text{Ca}_{3-x}\text{Ce}_x\text{Rh}_4\text{Sn}_{13}$ in a field-cooled (FC) and zero-field-cooled (ZFC) experiment with an applied field 0.05 T. The data are shown for $\text{Ca}_3\text{Rh}_4\text{Sn}_{13}$ (a) and for the compounds with $x = 0.2$ and 0.5 (b). The insets exhibit details in the extended χ axes.

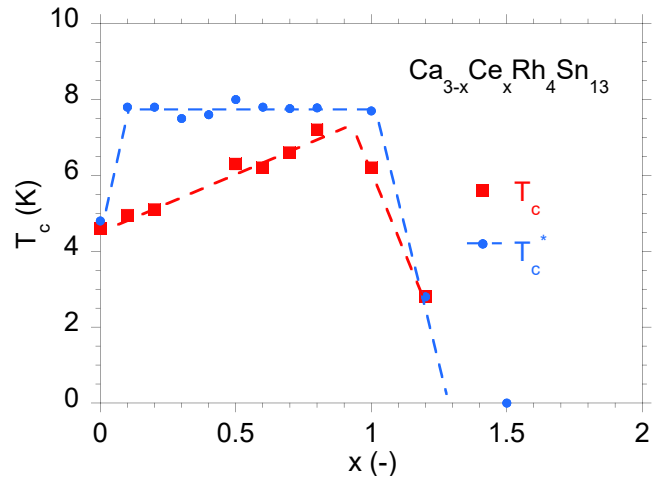


FIG. 5. Superconducting critical temperature T_c (red points) and T_c^* (blue points) of $\text{Ca}_{3-x}\text{Ce}_x\text{Rh}_4\text{Sn}_{13}$ for x from 0 to 1.2 obtained from χ_{ac} . An increase in Ce doping leads to an increase of the lattice constant (see Fig. 1c), suggesting an effective *chemical pressure* for the $x \leq 0$, undoped system (discussed later in the text).

ments of the dc magnetic susceptibility performed on the parent $\text{Ca}_3\text{Rh}_4\text{Sn}_{13}$ sample (cf. inset to Fig. 4a) reveal very weak thermal hysteresis in the ZFC and FC data between ~ 110 K and T_c . This is a significant phenomenon which may be interpreted in several ways. One interpretation could be the formation of a charge density wave (CDW) ordering or a structural distortion. There are a few examples of compounds that are isostructural to $\text{Ca}_3\text{Rh}_4\text{Sn}_{13}$, such as La-based²⁵ superconductors or $\text{Sr}_3\text{Ir}_4\text{Sn}_{13}$ superconductors^{14,26} which exhibit CDW ordering and structural distortions at about 100 – 140 K. Since the structural distortion has not been observed in $\text{Ca}_3\text{Rh}_4\text{Sn}_{13}$ ¹⁵, a weak spin fluctuation in $\text{Ca}_3\text{Rh}_4\text{Sn}_{13}$ could also explain the observed thermal hysteresis for $T_c < T < \sim 110$ K. The high temperature thermal hysteresis observed in χ_{dc} (Fig. 4a), χ_{ac} vs. frequency at $T < T_c$ and resistivity measurements (shown later) are also suggestive of a *granular effect*²⁷. This scenario seems to be very probable and will be discussed. In panel (b) of Fig. 4, χ can be well approximated by the modified Curie-Weiss expression $\chi = \chi_0 + C/(T + \theta_{CW})$ with Curie constant $C = 0.807$ K emu/mol Ce for Ce^{3+} ion, $\chi_0 = 3.7 \times 10^{-4}$ emu/mol Ce , and $\theta_{CW} = 31$ K, suggesting ferromagnetic correlations of Ce magnetic moments. For the similar isovalent compound $\text{Ca}_3\text{Ir}_4\text{Sn}_{13}$, there are a number of similar anomalies in the magnetic and electric transport properties at ~ 38 K which is well above the superconducting transition; these features were attributed to ferromagnetic spin fluctuations coupled to superconductivity^{28,29}, or a CDW effect³⁰. In order to study the complex interplay of magnetism and superconductivity in $\text{Ca}_{3-x}\text{Ce}_x\text{Rh}_4\text{Sn}_{13}$ with $x \leq 0.5$, we have investigated the ac mass magnetic susceptibility vs frequency and different ac amplitude of the magnetic field

(Figs 6 and 7). The perfect diamagnetism of the full Meissner state $\chi' = -1/(4\pi d) = 9.587 \times 10^{-3}$ emu/g for mass density $d = 8.3$ g/cm³³¹ is reached for Ca₃Rh₄Sn₁₃ below $T_c = 4.6$ K. The Ce doping and increasing amplitude of the magnetic field systematically reduces the Meissner effect about 73 % in Ca_{3-x}Ce_xRh₄Sn₁₃, which is for the ac magnetic field amplitude of 1 Oe at 2 K for the sample $x = 0.5$. The insets to Fig. 6 (lower panel)

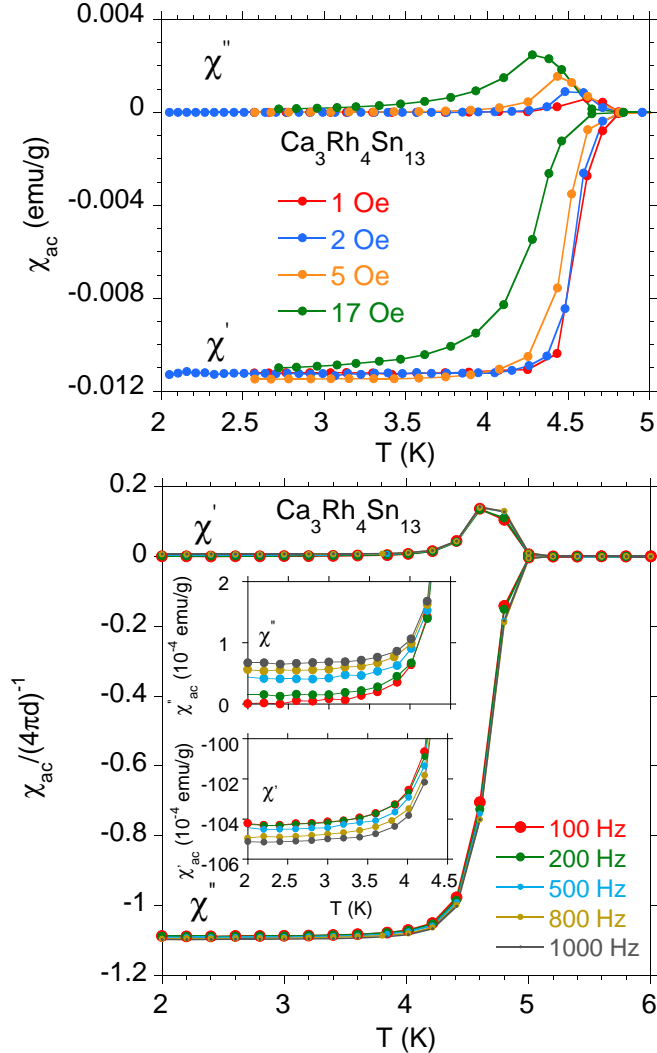


FIG. 6. The real and imaginary components of the ac magnetic susceptibility, χ' and χ'' , for Ca₃Rh₄Sn₁₃, as a function of temperature measured in various magnetic fields (a) and at different frequencies (b) in a field $B = 4$ Oe.

display weak frequency dependence of the real (χ') and imaginary (χ'') parts of ac mass magnetic susceptibility χ_{ac} , which could suggest an atomic disorder effect in Ca₃Rh₄Sn₁₃, while frequency and field dependencies in χ' and χ'' depicted in Fig. 7 become apparent for spin-glass-like behavior in Ce doped alloys.

Figure 8 shows the magnetization loops for the Ca_{3-x}Ce_xRh₄Sn₁₃ samples with $x \leq 0.5$ and the irreversibility in the magnetization curves observed for

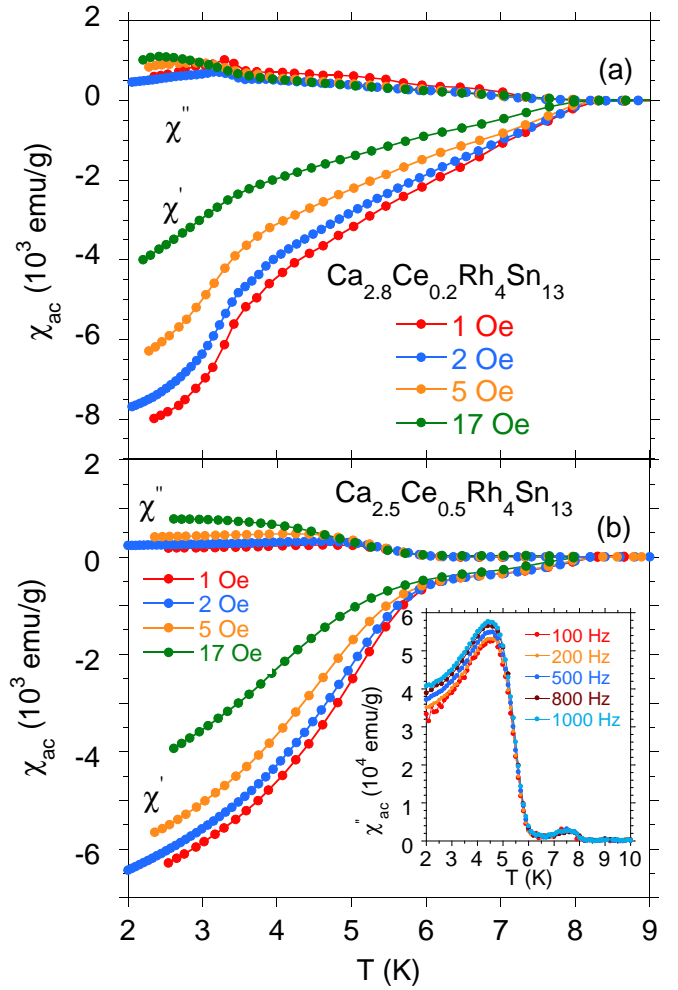


FIG. 7. The real and imaginary components of the ac magnetic susceptibility, χ' and χ'' , for Ca_{2.8}Ce_{0.2}Rh₄Sn₁₃ (a) and Ca_{2.5}Ce_{0.5}Rh₄Sn₁₃ (b), as a function of temperature measured in various magnetic fields. The inset to panel (b) shows how χ'' depends on frequency for Ca_{2.5}Ce_{0.5}Rh₄Sn₁₃ with evidence of the spin-glass state.

$T < T_c$ at lower fields represents the effect of vortex pinning. Moreover, Ca₃Rh₄Sn₁₃ is diamagnetic in the wide temperature region (Fig. 8a) with weak magnetization hysteresis loops observed at $T = 6, 10,$ and 50 K, which correlates with thermal hysteresis in the ZFC and FC χ data presented in Fig. 4a and is not associated with the flux pinning effect. For the alloys doped with Ce (cf. Fig. 8b), the magnetization M vs B isotherms for $B \gtrsim 1$ T are characteristic of paramagnets. The smaller hysteresis loop effect, as shown in the lower panel of Fig. 8, is likely due to atomic disorder and related to the more complicated effect of magnetic flux pinning.

A sharp superconducting transition in the specific heat data $C(T)/T$ at $T_c = 4.6$ K is shown for Ca₃Rh₄Sn₁₃ in Fig. 9a. The $C(T)/T$ data are well approximated by the expression $C(T)/T = \gamma + \beta T^2 + \frac{1}{T} A \exp(-\Delta_c(0)/k_B T)$. The best fit gives an electronic coefficient $\gamma = 6.1$ mJ/mol

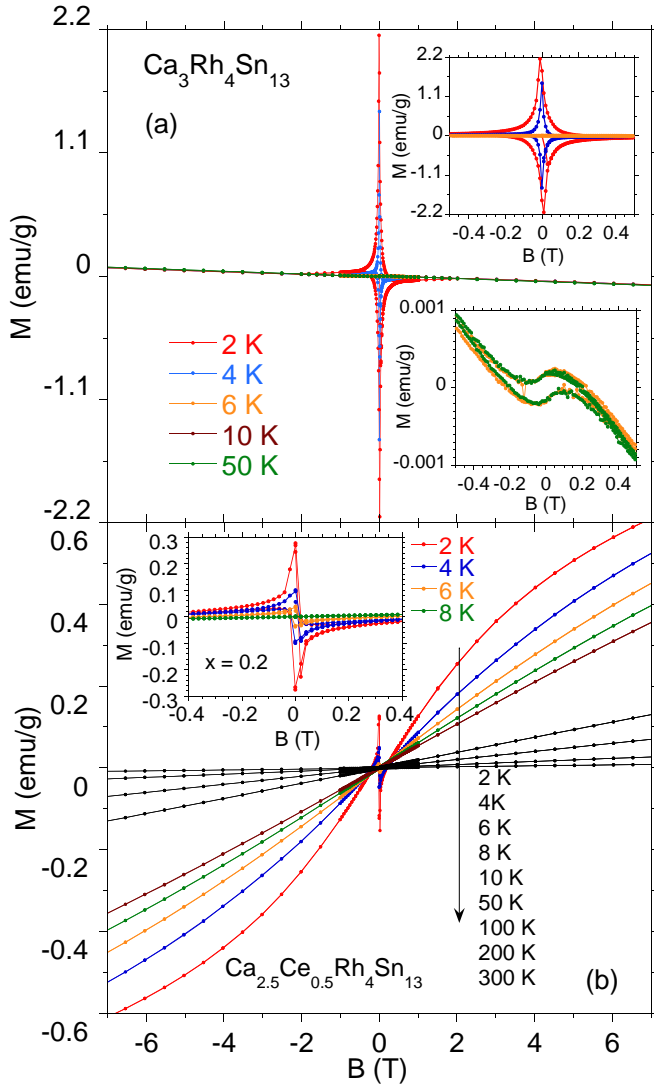


FIG. 8. Magnetization M vs magnetic field B for $\text{Ca}_3\text{Rh}_4\text{Sn}_{13}$ (a) and $\text{Ca}_{2.5}\text{Ce}_{0.5}\text{Rh}_4\text{Sn}_{13}$ (b) at different temperatures. The insets exhibit hysteresis loops at different temperatures.

K^2 , $\beta = 4 \text{ mJ/mol K}^4$ and the energy gap at $T = 0$, $\Delta_c(0)/k_B = 16.0 \text{ K}$. From $\beta = N(12/5)\pi^4 R\theta_D^{-3}$, we estimated the Debye temperature, $\theta_D \sim 213 \text{ K}$, which compares very well with the literature data³¹. The $C/T \sim \exp(-\Delta_c(0)/k_B T)$ exponential behavior indicates an s -wave and BCS character of superconductivity. We obtained $\Delta C/(\gamma T_c) \cong 1.4(7)$ based on a value of the electronic specific heat coefficient $\gamma = 34 \text{ mJ/mol K}^2$ for $T \leq T_c$ at a field of 3 T; we also determined $2\Delta_c(0)/k_B T_c \approx 7.0$ which is larger than that expected from the BCS theory ($2\Delta_c(0)/k_B T_c = 3.52$) which indicates that $\text{Ca}_3\text{Rh}_4\text{Sn}_{13}$ may be categorized as a strong coupling superconductor. The two lower panels, Fig. 9 (b) and (c) display the specific heat data $C(T)/T$ and $C(T)$, respectively, for $\text{Ca}_{2.8}\text{Ce}_{0.2}\text{Rh}_4\text{Sn}_{13}$. There is no sharp transition at T_c in the specific heat data shown in panel (b). Instead, the specific heat displays a broad peak

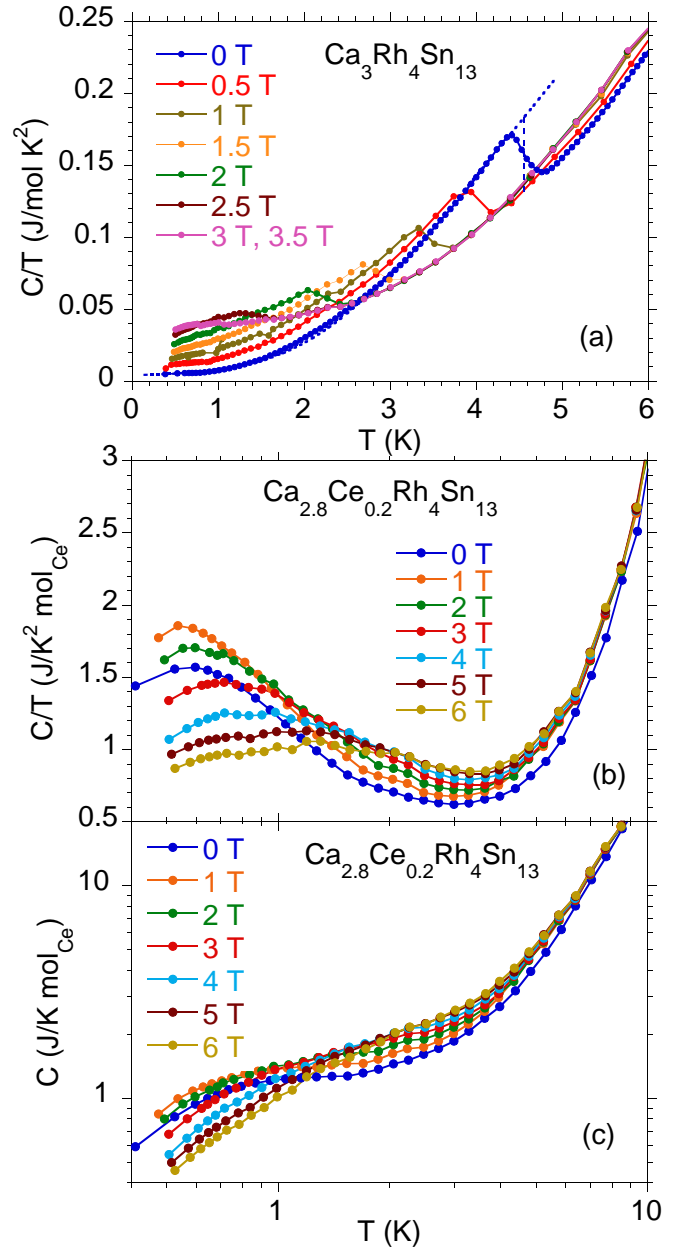


FIG. 9. (a) Temperature dependence of specific heat, $C(T)/T$, for $\text{Ca}_3\text{Rh}_4\text{Sn}_{13}$ in various magnetic fields. The dotted blue line is the best fit of the expression $C(T)/T = \gamma + \beta T^2 + \frac{1}{T} A \exp(-\Delta_c(0)/k_B T)$ to the data. The $C(T)/T$ and $C(T)$ data vs T at different magnetic fields are shown for $\text{Ca}_{2.8}\text{Ce}_{0.2}\text{Rh}_4\text{Sn}_{13}$ in panel (b) and (c), respectively.

at $T \approx 0.6 \text{ K}$ with a maximum value of $C/T = 1.9 \text{ J/K}^2 \text{ mol}_{\text{Ce}}$ which is strongly reduced by field, shifts to higher temperatures, and is not related to the superconductivity of the sample. We attribute this low-temperature C behavior to the formation of a spin-glass-like magnetic state. The low- T heat capacity gives magnetic entropy $S = 1 \text{ J/K mol}_{\text{Ce}}$, while the limit $S = R \ln 2$ ³² is reached at about 6 K, well above the C/T maximum. If the cause of the maximum in C and C/T was due solely to a

Kondo effect, then C/T should be about $4 \text{ J/K}^2 \text{ mol}_{\text{Ce}}^{-33}$ in the limit of $T \rightarrow 0$ (recently we have shown a single ion Kondo impurity state for La-diluted isostructural $\text{Ce}_{3-x}\text{La}_x\text{Co}_4\text{Sn}_{13}$ ³³ and $\text{Ce}_{3-x}\text{La}_x\text{Rh}_4\text{Sn}_{13}$ ²⁴ series of compounds with small value of Kondo temperature of about 1.5 K and $C(T)/T$ value almost not x -dependent and about $3-4 \text{ J/K}^2 \text{ mol}_{\text{Ce}}^{-1}$). Moreover, the $4f$ contribution to the specific heat, $\Delta C(T)$, should be approximated by the Kondo resonant-level model³⁴, however, this is not a case. Within this model the Kondo-impurity contribution to ΔC can be described by the expression:

$$\Delta C = R \frac{2S\Delta_K}{\pi k_B T} - 2RRe \left\{ \frac{(\Delta_K + ig\mu_B H)^2}{(2\pi k_B T)^2} \right. \\ \times \left[(2S+1)^2 \psi' \left(1 + \frac{\Delta_K + ig\mu_B H}{2\pi k_B T} (2S+1) \right) \right. \\ \left. \left. - \psi' \left(1 + \frac{\Delta_K + ig\mu_B H}{2\pi k_B T} \right) \right] \right\}, \quad (1)$$

where ψ' is the first derivative of the digamma function, and Δ_K/k_B is of the order of the Kondo temperature T_K . The best approximation gives $\Delta_K = 0$, which eliminates the Kondo impurity effect as dominant. Therefore, the $C(T)$ and $\chi_{ac}(T)$ data for $\text{Ca}_{2.8}\text{Ce}_{0.2}\text{Rh}_4\text{Sn}_{13}$ indicate the coexistence of an inhomogeneous superconducting phase (cf. Ref. 8 and 9) and a spin-glass-like state at temperatures below T_c . Very recently we have discussed a very similar specific heat behavior in so strongly disordered $\text{La}_3\text{Co}_x\text{Ru}_{4-x}\text{Sn}_{13}$ superconductors⁹ that the expected specific heat jump and the onset of diamagnetism are spread out over a very large temperature range. It has been shown that potential disorder smooth on a scale comparable to the coherence length leads to large modulation of the superconducting gap and large transition width, similar to that shown in Fig. 7.

Figure 10 displays the zero field electrical resistivity ρ between 0.4 and 300 K for $\text{Ca}_{3-x}\text{Ce}_x\text{Rh}_4\text{Sn}_{13}$ compounds, normalized to the value of ρ at $T = 300 \text{ K}$. The samples $0 \leq x \leq 0.5$ show a superconducting transition. The remaining compounds in the series for which $x > 0.5$ exhibit $\rho(T)$ that is characteristic of Kondo-lattice systems, with distinct anomalies at $T \approx 160 \text{ K}$ for the samples $x = 2.5$ and 2.8 due to a subtle deformation of the Sn_{12} cages (cf. Refs. 33 and 35, and Fig. 2). Now we will discuss the $\rho(T)$ data for the superconducting samples. Figure 11 shows the temperature dependence of the electrical resistivity for $x = 0, 0.2$ and 0.5 . The transitions in the doped samples are much broader than for the $x = 0$ compound, which shows that substitution of Ce for Ca introduces inhomogeneity into the system. It is interesting to note the shape of $\rho(T)$ for $x = 0.5$ which exhibits two clear separate drops in ρ , one near $T_{c1} = 8 \text{ K}$ and another near $T_{c2} = 6.7 \text{ K}$. T_{c1} coincides with the temperature of the single transition for $x \gtrsim 1$. The two distinct drops in ρ for $x = 0.5$ indicate a double resistive phase transition to the superconducting state. Such a double transition is typical for inhomogeneous (granular) superconductors³⁶, in which isolated superconducting *islands* are formed at

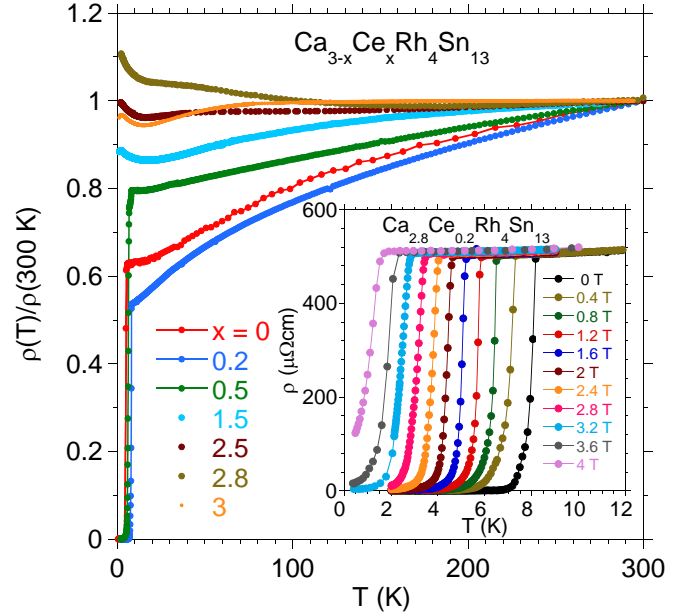


FIG. 10. Electrical resistivity $\rho(T)$ normalized by its room temperature value for $\text{Ca}_{3-x}\text{Ce}_x\text{Rh}_4\text{Sn}_{13}$ compounds. The inset shows the temperature dependence of ρ for $\text{Ca}_{2.8}\text{Ce}_{0.2}\text{Rh}_4\text{Sn}_{13}$ at various externally applied magnetic fields.

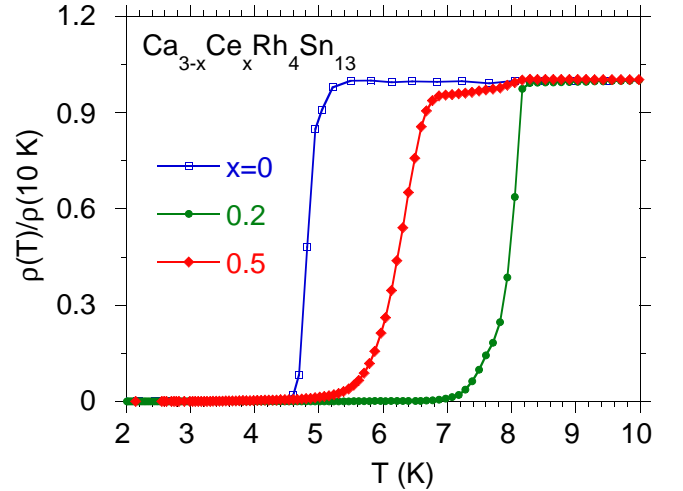


FIG. 11. Electrical resistivity of the superconducting $\text{Ca}_{3-x}\text{Ce}_x\text{Rh}_4\text{Sn}_{13}$ samples ($x = 0, 0.2$, and 0.5) normalized to ρ at $T = 10 \text{ K}$, near the critical temperature T_c .

the higher temperature, T_{c1} . Then, at the lower temperature, T_{c2} , a global phase coherence develops at which point $\rho \rightarrow 0$. The double transition can also be seen in the ac susceptibility (see Fig. 7b): χ' starts to diminish at $T = 8 \text{ K}$, but significantly decreases only for $T < 6 \text{ K}$. Additionally, the anomaly in χ'' seen for temperatures between 6 K and 8 K (the inset in Fig. 7b) can be interpreted as a signature of the double transition³⁷.

The inset in Fig. 10 displays $\rho(T)$ for $\text{Ca}_{2.8}\text{Ce}_{0.2}\text{Rh}_4\text{Sn}_{13}$ in various magnetic fields. The

$\rho(T)$ data exhibits a sharp transition near T_c which is very similar to the behavior at T_c that was observed for $\text{Ca}_3\text{Rh}_4\text{Sn}_{13}$ and $\text{Ca}_{2.5}\text{Ce}_{0.5}\text{Rh}_4\text{Sn}_{13}$. In Fig. 12, we show the $H - T$ phase diagram, where the critical temperatures were determined to be the temperature at which ρ reaches 50% of its value in the normal state. For the $\text{Ca}_3\text{Rh}_4\text{Sn}_{13}$ compound, there is also evidence of two superconducting phases, however, the nature of these transitions is different from that for $\text{Ca}_{2.5}\text{Ce}_{0.5}\text{Rh}_4\text{Sn}_{13}$. There is only one drop of resistivity, but its temperature is slightly off the position of the peak in the specific heat. A similar situation was observed in $\text{La}_3\text{Rh}_4\text{Sn}_{13}$ ⁸ and $\text{La}_3\text{Ru}_4\text{Sn}_{13}$ ⁹. The transitions are represented in Fig. 12 by the $H - T$ curves (a) and (b); the data points along the (a) and (b) curves were obtained from the resistivity (T_c^* inhomogeneous phase) and specific heat (T_c phase) data, respectively. The $H - T$ data from all samples

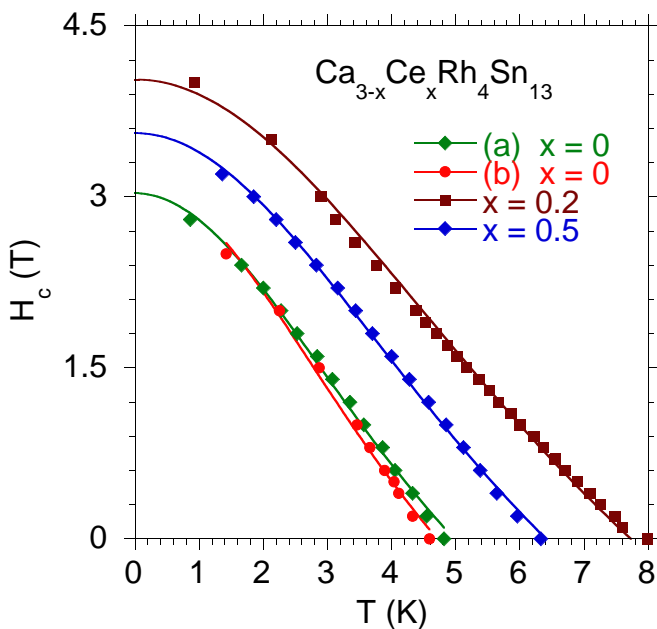


FIG. 12. Temperature dependence of the upper critical field H_{c2} in the $H - T$ phase diagram for $\text{Ca}_3\text{Rh}_4\text{Sn}_{13}$ (symbols a and b), $\text{Ca}_{2.8}\text{Ce}_{0.2}\text{Rh}_4\text{Sn}_{13}$, $\text{Ca}_{2.5}\text{Ce}_{0.5}\text{Rh}_4\text{Sn}_{13}$, respectively. T_c values characterized by points a for $\text{Ca}_3\text{Rh}_4\text{Sn}_{13}$, and for the samples $x = 0.2$ and 0.5 are obtained from electrical resistivity data under H , and defined as the temperature at which ρ drops to 50% of its normal-state value. The red symbols b represent T_c obtained from $C(T)/T$ vs T data in Fig. 9. The solid color lines represent a fit using the Ginzburg-Landau model of $H_{c2}(T)$.

are well approximated by the Ginzburg-Landau (GL) theory. The best fit of equation $H_{c2}(T) = H_{c2}(0) \frac{1-t^2}{1+t^2}$, where $t = T/T_c$ gives the upper critical field values of $H_{c2}(0)$ and $H_{c2}^*(0) \sim 3.1$ T for $\text{Ca}_3\text{Rh}_4\text{Sn}_{13}$, $H_{c2}^*(0) = 3.6$ T for $\text{Ca}_{2.8}\text{Ce}_{0.2}\text{Rh}_4\text{Sn}_{13}$, and $H_{c2}^*(0) = 4.0$ T for $\text{Ca}_{2.5}\text{Ce}_{0.5}\text{Rh}_4\text{Sn}_{13}$. The critical temperatures determined from the best fit of the GL equation to the $H - T$ plots are: $T_c = 4.71$ K and $T_c^* = 4.97$ K for

$\text{Ca}_3\text{Rh}_4\text{Sn}_{13}$, $T_c^* = 7.73$ K, and $T_c = 6.41$ K for the samples substituted with nominal Ce concentrations of $x = 0.2$ and $x = 0.5$, respectively. Using the Ginzburg-Landau relation³⁸ $\mu_0 H_{c2}(0) = \Phi_0/2\pi\xi(0)^2$ we determined the superconducting coherence length $\xi(0)$, where $\Phi_0 = h/2e = 2.068 \times 10^{-15}$ Tm² is the flux quantum. $\text{Ca}_3\text{Rh}_4\text{Sn}_{13}$ exhibits similar values of $\xi(0)$ and $\xi(0)^* \cong 10.3$ nm; for $\text{Ca}_{2.8}\text{Ce}_{0.2}\text{Rh}_4\text{Sn}_{13}$, $\xi(0)^* \cong 9.6$ nm, and for $\text{Ca}_{2.5}\text{Ce}_{0.5}\text{Rh}_4\text{Sn}_{13}$, $\xi(0)^* \cong 9.0$ nm. In Fig. 12, all these $H_c(T)$ curves have a small initial positive curvature. This feature can also be found in other skutterudites, such as $\text{PrOs}_4\text{Sb}_{12}$ ³⁹. It is interesting that this compound also exhibits a double superconducting transition, but it was claimed in Ref. 40 that the positive curvature of $H_{c2}(T)$ is not related with sample inhomogeneities. A similar shape of $H_{c2}(T)$ also appears in MgB_2 ,⁴¹ in borocarbides such as $\text{YNi}_2\text{B}_2\text{C}$ and LuNi_2B_2 ,⁴² or in the cuprates.⁴³

The pressure (P) evolution of the electrical resistivity as a function of temperature for $\text{Ca}_3\text{Rh}_4\text{Sn}_{13}$ and $\text{Ca}_{2.8}\text{Ce}_{0.2}\text{Rh}_4\text{Sn}_{13}$ is displayed in Figs. 13 and 14, respectively. From these data we obtained the pressure coefficients $\frac{dT_c}{dP}$ or $\frac{dT_c^*}{dP}$ and $\frac{d\rho}{dP}$. (i) The pressure coefficients of T_c^* are -0.2 K/GPa for $\text{Ca}_3\text{Rh}_4\text{Sn}_{13}$ and -0.3 K/GPa for the $x = 0.2$ sample substituted with Ce. These values of $\frac{dT_c^*}{dP}$ are about twice those values for T_c , are found in similar isostructural La-based superconductors (cf. Ref. 9), and seems to be characteristic of materials which show evidence of nanoscale disorder leading to an inhomogeneous superconducting state with $T_c^* > T_c$.

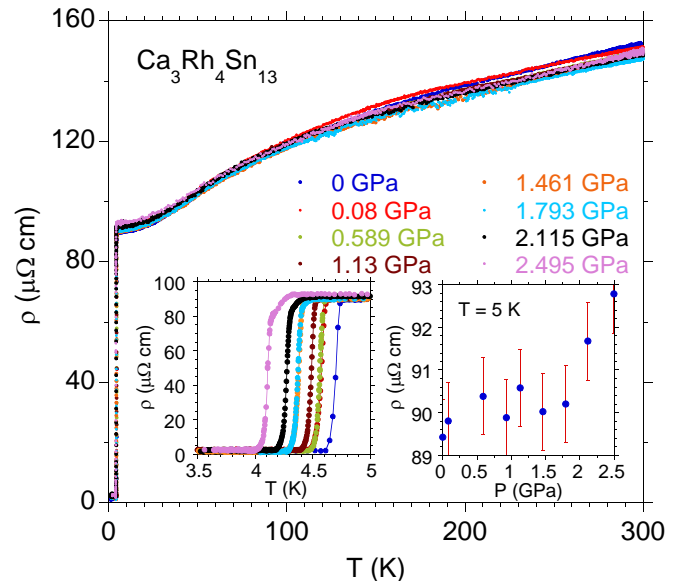


FIG. 13. Electrical resistivity for $\text{Ca}_3\text{Rh}_4\text{Sn}_{13}$ under applied pressure. The left inset shows the details near the critical temperature. The right inset displays the value of ρ measured just above T_c at $T = 5$ K.

Within the Eliashberg theory of strong-coupling

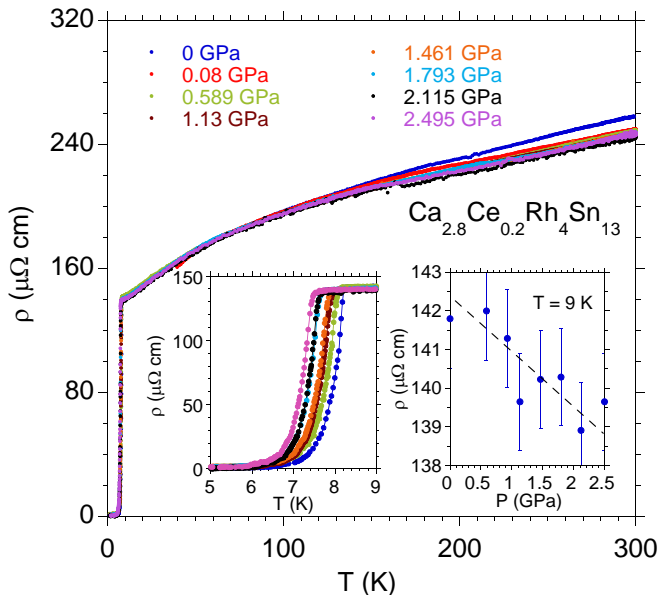


FIG. 14. Electrical resistivity for $\text{Ca}_{2.8}\text{Ce}_{0.2}\text{Rh}_4\text{Sn}_{13}$ under applied pressure. The left inset shows the details near the critical temperature. The right inset displays the value of ρ measured just above T_c at $T = 9$ K.

superconductivity,⁴⁴ the McMillan expression,^{45,46}

$$T_c = \frac{\theta_D}{1.45} \exp \left\{ \frac{-1.04(1 + \lambda)}{\lambda - \mu^*(1 + 0.62\lambda)} \right\}, \quad (2)$$

as a solution to the finite-temperature Eliashberg equations, gives an estimate of the electron-phonon coupling parameter $\lambda \approx 0.62$ (for T_c^* phase $\lambda^* \approx 0.63$), when the Coulomb repulsion μ^* is assumed to be ~ 0.1 as a typical value known for s and p band superconductors. The electron-phonon coupling λ is given by the expression^{45,47},

$$\lambda = \frac{N(E_F)\langle I^2 \rangle}{M\langle \omega^2 \rangle}, \quad (3)$$

where $\langle I^2 \rangle$ is the square of the electronic matrix element of electron-phonon interactions averaged over the Fermi surface, $\langle \omega^2 \rangle$ is an average of the square of the phonon frequency, and M is the atomic mass, is larger for the inhomogeneous superconducting T_c^* state with respect to the bulk effect observed below T_c , which may lead to a larger value of $\frac{dT_c^*}{dP}$ than $\frac{dT_c}{dP}$. The primary reason for $\frac{dT_c^*}{dP} > \frac{dT_c}{dP}$ is the pressure dependence of θ_D , which leads to larger lattice stiffening in the T_c^* phase with respect to the bulk effect below T_c and contributes to the $T_c^* > T_c$ effect. The dependence is given by the Grüneisen parameter $\gamma_G = -\frac{d\ln\theta_D}{d\ln V}$, which determines the lattice stiffening. Using the McMillan expression it was found⁴⁸ that γ_G strongly determines the magnitude and sign of dT_c/dP . It is also probable that in the case of inhomogeneous superconductivity, the pressure dependence of the density of states at the Fermi level is more pronounced

than in bulk superconductors, and may lead to a larger value of dT_c^*/dP than dT_c/dP . (ii) For $T > T_c$, the electrical resistivity (Fig. 13) shows the positive coefficient $\frac{d\rho}{dP}$ for $\text{Ca}_3\text{Rh}_4\text{Sn}_{13}$, while for the Ce doped sample (Fig. 14) $\frac{d\rho}{dP} < 0$. This diverse ρ vs P behavior is interpreted as a result of the pressure dependent band structure near the Fermi energy (which will be discussed below).

2. Band structure of $\text{Ca}_3\text{Rh}_4\text{Sn}_{13}$ under pressure

Figure 15 compares the valence band X-ray photoelectron spectroscopy (VB XPS) spectra for $\text{Ca}_3\text{Rh}_4\text{Sn}_{13}$ and the calculated bands. The ground state is calculated as nonmagnetic. A comparison of the theoretical and experimental results shows that the calculated density of states (DOS) reflects all of the features found in the VB XPS spectra for $\text{Ca}_3\text{Rh}_4\text{Sn}_{13}$. The most intense peak at about 3 eV originates mainly from the Rh 4d states which are hybridized with the 5p states of Sn2. The inset exhibits a maximum in the DOS at the Fermi energy with a significant contribution coming from the Sn2 5p states, which suggests the importance of these electronic states in electric transport.

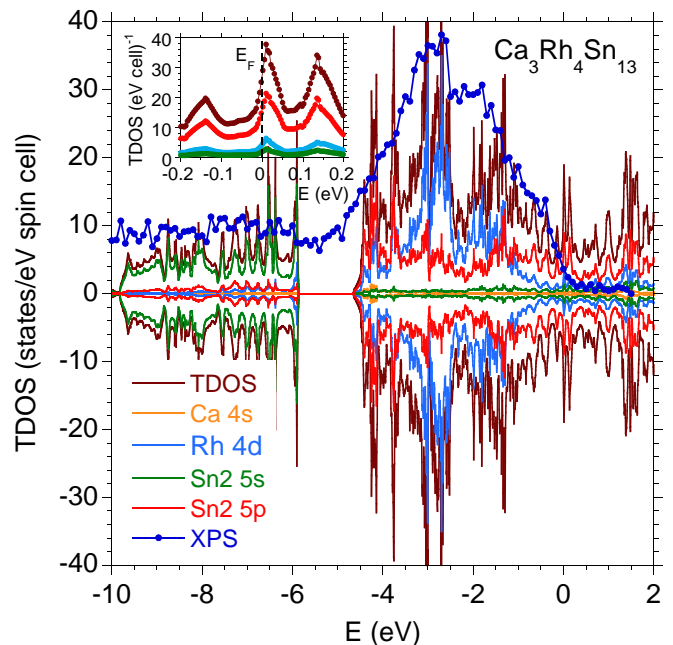


FIG. 15. Valence band XPS spectrum for $\text{Ca}_3\text{Rh}_4\text{Sn}_{13}$ compared with the calculated total and spin-resolved density of states within the LSDA approximation. The figure also shows Ca 4s, Rh 4d, Sn2 5p and 5s states for $\text{Ca}_3\text{Rh}_4\text{Sn}_{13}$. The inset exhibits the energy distribution of these partial DOS near the Fermi energy.

In order to understand the effect of pressure on the band structure, the DOS calculations were performed for hypothetical lattice parameters that are smaller compared to the parameters that were measured at room

temperature. We used the Birch-Murnaghan isothermal equation of state⁴⁹ to estimate the hypothetical applied pressure that would correspond to a systematic decrease in the unit cell volume: $V(P) = V(0)[1 + \frac{B'}{B}P]^{-1/B'}$, where $V(0)$ is the unit cell volume experimentally obtained at room temperature and ambient pressure, $B = 91.64$ GPa is the calculated bulk modulus, and $B' = 4.95$ is its pressure derivative. Figure 16 displays the calcu-

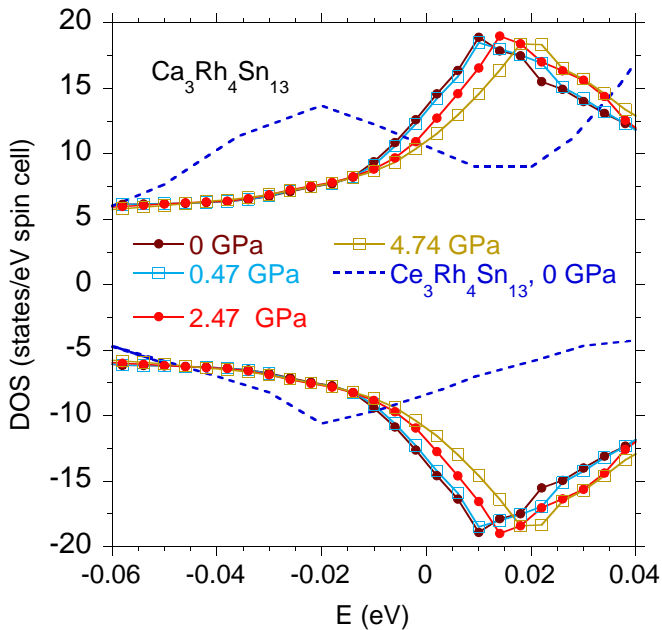


FIG. 16. The total and spin-resolved density of states near the Fermi energy within the LSDA approximation at various pressures, calculated for $\text{Ca}_3\text{Rh}_4\text{Sn}_{13}$. The dotted blue line represents the total DOS calculated for $\text{Ce}_3\text{Rh}_4\text{Sn}_{13}$.

lated DOS at various pressure. There is a systematic change in the DOS vs P near E_F . However, it is interesting to note the change in the DOS vs P at the Fermi energy as an explanation for the observed coefficient $\frac{d\rho}{dP} > 0$, shown for $\text{Ca}_3\text{Rh}_4\text{Sn}_{13}$ in Fig. 13. Our calculations documented the linear decrease of the total DOS at E_F with P in the region of $P < 4.5$ GPa, giving $\frac{d(\text{DOS})}{dP} \cong -1.3 \text{ eV}^{-1} \text{ GPa}^{-1}$ (the proper DOSs taken from Fig. 13), which correlates well with the observed positive $\frac{d\rho}{dP} \cong 1.2 \mu\Omega \text{ GPa}^{-1}$ at applied pressure $P < 2.5$ GPa. This simple estimate bases on the relation $\rho \sim 1/n$ between the resistivity and the number of carriers n , that naively reflects the DOS at the Fermi level. Moreover, the value of $\frac{d(\text{DOS})}{dP}$ roughly agrees with the pressure dependence of ρ in the limit of low T .

Secondly, a linear change of the calculated $\text{DOS}(P)$ at E_F with the change of the lattice parameter a was obtained on the basis of the Birch-Murnaghan isothermal equation of state. Namely, the calculated DOS decreases with decreasing volume of the sample. Assuming that this linearity is extended to the region of *negative* lattice pressure (as is the case for $\text{Ca}_3\text{Rh}_4\text{Sn}_{13}$ with $T_c \sim 8$ K,

cf. Fig. 1 and Ref. 17) and that U does not strongly depend on P , we attempt to demonstrate how the change in DOS would increase T_c for $\text{Ca}_3\text{Rh}_4\text{Sn}_{13}$. This would follow from the BCS equation⁵⁰ $T_c = \theta_D e^{-1/\text{DOS}(E_F)U}$ and the expression for the DOS : $\text{DOS}(E_F)U \sim \frac{\lambda - \mu^*}{1 + \lambda}$ ⁵¹. We considered the calculated DOS for our sample with $T_c = 4.8$ K at ambient pressure in order to estimate the value of U . A simple approximation gives $T_c \approx 10$ K, which is comparable to the value of $T_c \sim 8.4$ K that was found experimentally for the as-grown sample (cf. Fig. 1 and Ref. 17).

The proposed model explains too the higher value of $T_c^* = 8$ K which was documented experimentally for the $\text{Ca}_{3-x}\text{Ce}_x\text{Rh}_4\text{Sn}_{13}$ samples with $0 < x < 1$ compared to the parent compound $\text{Ca}_3\text{Rh}_4\text{Sn}_{13}$ with $T_c^* = 4.9$ K. For $\text{Ca}_{2.8}\text{Ce}_{0.2}\text{Rh}_4\text{Sn}_{13}$, one can expect an increase of the DOS at E_F caused by either the presence of Ce f -states (cf. Fig. 16 displays the total DOS for isostructural $\text{Ce}_3\text{Rh}_4\text{Sn}_{13}$) or a larger lattice parameter (as is shown in Fig. 1) than what was observed in the parent compound. Within our model, even a slight increase in the DOS at E_F may cause a significant increase in T_c for $\text{Ca}_{2.9}\text{Ce}_{0.1}\text{Rh}_4\text{Sn}_{13}$ relative to the value of T_c observed for the parent compound $\text{Ca}_3\text{Rh}_4\text{Sn}_{13}$. It is apparent that the external pressure shifts the DOS of $\text{Ce}_3\text{Rh}_4\text{Sn}_{13}$ toward the Fermi energy and therefore one can expect an effective increase in the total DOS at E_F with increasing P for Ce-doped alloys as well. This behavior correlates well with the observed negative $\frac{d\rho}{dP}$ at low T , as is shown in the inset of Fig. 14.

Previously we discussed the effect of nanoscale disorder leading to an inhomogeneous superconducting state with the critical temperature T_c^* higher than T_c of the bulk phase. This scenario seems, however, not to be adequate for $\text{Ca}_3\text{Rh}_4\text{Sn}_{13}$, where the difference $T_c^* - T_c \sim 0.1$ K is small and hardness of the both superconducting phases is very similar. We can not, however, exclude the impact of the disorder on the T_c^* of Ce-doped alloy, as an additional effect, evident in temperature dependence of the specific heat. It was shown theoretically^{52,53} and experimentally^{2,54} that the superconducting transition temperature is higher in the presence of the spin-glass state compared to the noninteracting case. Generally, disorder can either suppress or significantly increase T_c values⁵⁵. The Ce-doped $\text{Ca}_3\text{Rh}_4\text{Sn}_{13}$ seems to be an example of strong-coupling superconductor with the spin-glass-like state documented experimentally and generated by an atomic disorder.

3. Bonding properties of $\text{Ce}_3\text{Rh}_4\text{Sn}_{13}$ investigated by electron localization function, absence of structural distortion

For the series of skutterudite-related compounds, $\text{Ce}_3M_4\text{Sn}_{13}$ and $\text{La}_3M_4\text{Sn}_{13}$, where M is a d -electron metal, the charge density analysis revealed a strong charge accumulation between the M and Sn2 atoms, which implies a strong covalent bonding interaction and

leads to a subtle structural transition at $T_D \sim 150$ K⁵⁶. In this class of materials, the structural deformation is usually accompanied by formation of a charge density wave (CDW) phase transition, and under external pressure $T_D \rightarrow 0$ defines a novel structural quantum critical point¹⁴. The structural deformation, however, was not documented for $\text{Ca}_3\text{Rh}_4\text{Sn}_{13}$. To determine the subtle bonding properties of the charge distribution in $\text{Ca}_3\text{Rh}_4\text{Sn}_{13}$ we present a full-potential chemical-bonding analysis via calculation of the electron localization function within the density functional theory.⁵⁷ The ELF distribution is given by $\eta(\vec{r}) = [1 + \chi^2(\vec{r})]^{-1}$, where

$$\chi(\vec{r}) = \frac{\frac{1}{2} \sum_i |\vec{\nabla} \psi_i|^2 - \frac{1}{8} \frac{(\vec{\nabla} \rho)^2}{\rho}}{\frac{3}{10} (3\pi^2)^{2/3} \rho^{5/3}}. \quad (4)$$

$\vec{\nabla} \psi_i(\vec{r}) \equiv \psi_{\nu\vec{k}}(\vec{r})$ are the crystal wave functions with band index ν and wavevector \vec{k} , and $\rho(\vec{r})$ is the total charge density. ELF isosurfaces are shown in Fig. 17a.

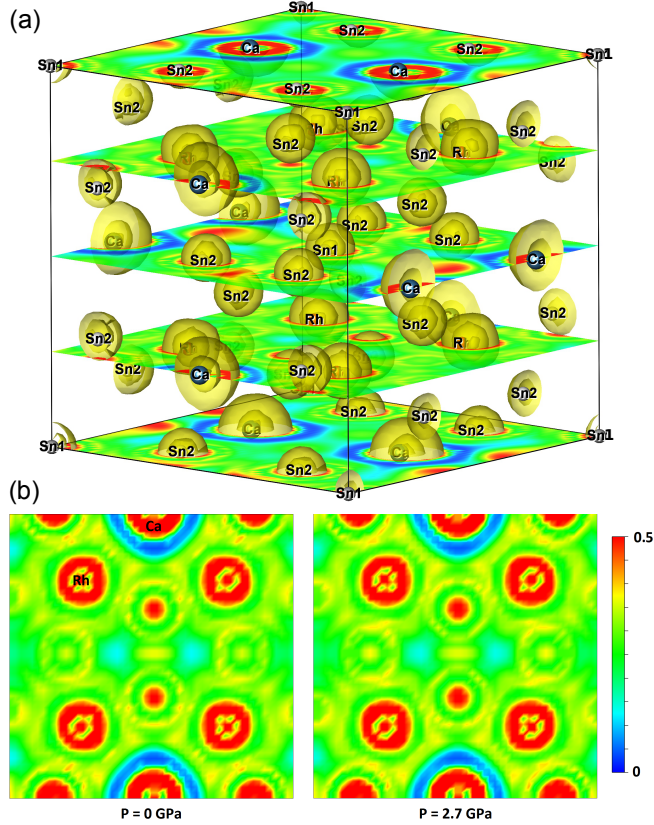


FIG. 17. (a) ELF isosurfaces for $\text{Ca}_3\text{Rh}_4\text{Sn}_{13}$. (b) The ELF distribution in the plane $(00\frac{1}{4})$ for $\text{Ca}_3\text{Rh}_4\text{Sn}_{13}$ calculated for $P = 0$ and 2.7 GPa. Note, that the pressure up to 2.7 GPa does not change the ELF distribution.

Figure 17b exhibits the ELF distribution in the plane $(00\frac{1}{4})$ for $\text{Ca}_3\text{Rh}_4\text{Sn}_{13}$. The ELF maxima are located on the atoms in the plane, but the covalent bonding between Rh and Sn atoms, characteristic of $\text{Ce}_3\text{M}_4\text{Sn}_{13}$ and

$\text{La}_3\text{M}_4\text{Sn}_{13}$ counterparts⁵⁶ are not observed. This covalent bonding is a cause of structural distortion at $T_D \sim 100 - 160$ K in the $\text{Ce}_3\text{M}_4\text{Sn}_{13}$ and $\text{La}_3\text{M}_4\text{Sn}_{13}$ compounds. This superlattice transition that is connected to a CDW instability of the conduction electron system which is observed in most of these compounds is not observed in $\text{Ca}_3\text{Rh}_4\text{Sn}_{13}$. For $\text{Ca}_3\text{Rh}_4\text{Sn}_{13}$, the ELF analysis also confirms that the thermal hysteresis present in χ as shown in Fig. 4 is not of the CDW origin but results rather from the inhomogeneity of the sample.

IV. ELECTRONIC STRUCTURE AND MAGNETIC PROPERTIES OF $\text{Ca}_{3-x}\text{Ce}_x\text{Rh}_4\text{Sn}_{13}$ WITH KONDO LATTICES FOR $x \geq 1.5$

In order to explain the (de)localized character of the Ce $4f$ -electron states in the system of $\text{Ca}_{3-x}\text{Ce}_x\text{Rh}_4\text{Sn}_{13}$ alloys we analyze the valence band and the Ce- $3d$ core level XPS spectra. The VB XPS bands shown in Fig. 18a are very similar across the series x of compounds we investigated, which suggests that the Rh $4d$ -electron states dominate the shape of the bands, while the $4f$ -electron state contribution is small. This behavior is typical for isostructural compounds $\text{RE}_3\text{M}_4\text{Sn}_{13}$. The LSDA calculations (cf. Fig. 15) support these experimental observations. In panel (b) of Fig. 18, the Ce- $3d$ core level XPS spectra demonstrate the well localized Ce $4f$ -electron states and the weak hybridization between the Ce $4f$ -electron and conduction band states, characterized by energy Δ . The qualitative analysis of the $3d$ XPS spectra shown in Fig. 18b was performed based on the Gunnarsson and Schönhammer theoretical method. The model (for details see Refs. 58–60) explains a complex structure of the Ce- $3d$ core level XPS spectra in which the main $3d^9_{5/2}4f^1$ and $3d^9_{3/2}4f^1$ spin-orbit splitting components of the final states are associated with the stable configuration of the Ce- $4f$ shell and the contributions from the $3d^94f^0$ and $3d^94f^2$ are due to on-site hybridization between the f -electron states and conduction band. The presence of the $3d^94f^0$ satellite line usually indicates an intermediate valence of the Ce ions, while $3d^94f^2$ reflects the hybridization effect which is expressed by energy $\Delta = \pi V^2 \text{DOS}(\epsilon_F)$. Standard analysis of the intensities of the components of the Ce- $3d$ XPS spectra shown in Fig. 18b suggests both the presence of Ce^{3+} ions⁶¹ and also a small hybridization energy $\Delta \approx 80 \pm 20$ meV.

Our complex research suggests there is single-ion Kondo behavior in $\text{Ca}_{3-x}\text{Ce}_x\text{Rh}_4\text{Sn}_{13}$. Figure 19 shows the low-temperature specific heat of $\text{Ca}_{1.5}\text{Ce}_{1.5}\text{Rh}_4\text{Sn}_{13}$ as $C(T)$ in panel (a) and $C(T)/T$ in panel (b) as well as the low-temperature specific heat as $C(T)/T$ in panel (c) for the $\text{Ca}_{0.2}\text{Ce}_{2.8}\text{Rh}_4\text{Sn}_{13}$ compound. The large value of $C(T)/T \sim 4$ J/K² mol_{Ce} for $T \rightarrow 0$ is typical for the family of $\text{Ce}_3\text{M}_4\text{Sn}_{13}$ heavy Fermi liquids (c.f. Refs.^{24,33}). Moreover, the $4f$ -electron contribution to the specific heat C is well approximated by the Kondo resonant-level

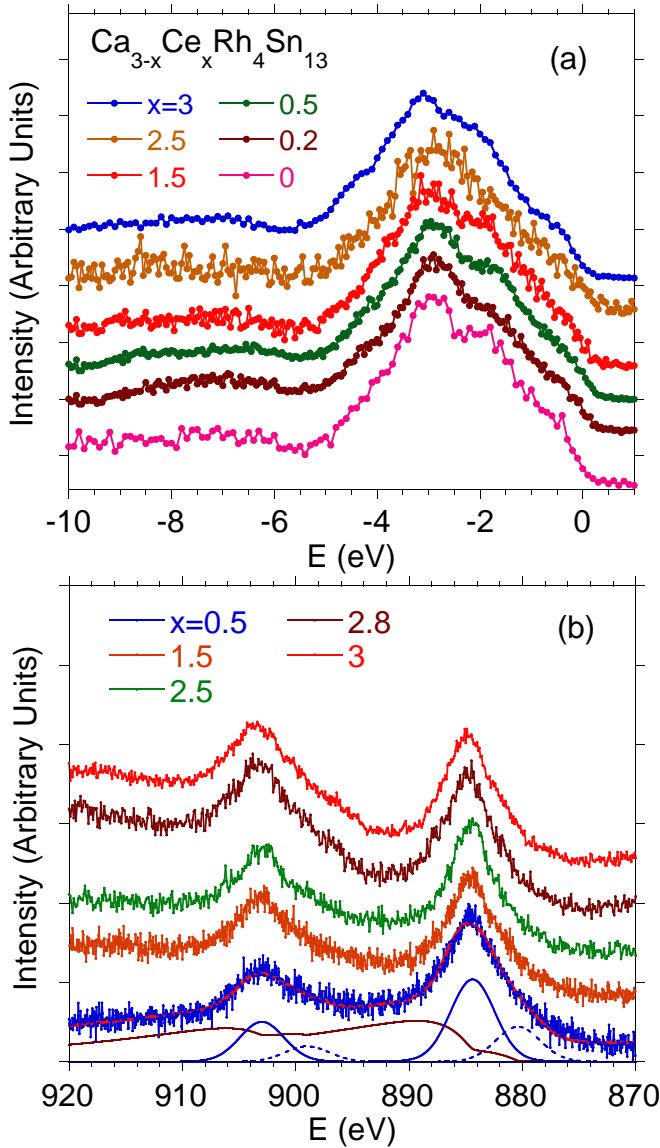


FIG. 18. (a) Valence-band XPS spectra for $\text{Ca}_{3-x}\text{Ce}_x\text{Rh}_4\text{Sn}_{13}$, which show very similar structure across the series x . (b) The Ce 3d XPS spectra at the room temperature exhibit a deconvoluted spectrum for $\text{Ca}_{2.5}\text{Ce}_{0.5}\text{Rh}_4\text{Sn}_{13}$ on the basis of the Gunnarsson-Schönhammer theoretical model, as an example, with spin-orbit components $3d^9 4f^0$ (blue solid line) and $3d^9 4f^2$ (blue dotted line). The brown solid line represents the background, the solid red line shows the fit after deconvolution to the XPS spectra. (From the deconvolution procedure, the Sn 3s line contribution at 885 eV provides about 15 % of the total peak intensity due to $3d_{5/2}^9 4f^1$ final states.)

model. In Fig. 19a we present the fit of the expression $C(T) = \gamma_0 T + \beta T^3 + \Delta C$ to the experimental data, where ΔC is defined in Eq. 1. The level width $\Delta_K/k_B \approx 0.95$ K for $B = 0$ and is found to increase with magnetic field ($\Delta_K/k_B \approx 2.25$ K for $B = 6T$). This behavior is characteristic of a single-ion Kondo system. Figure 20 shows the temperature dependence of the dc magnetic

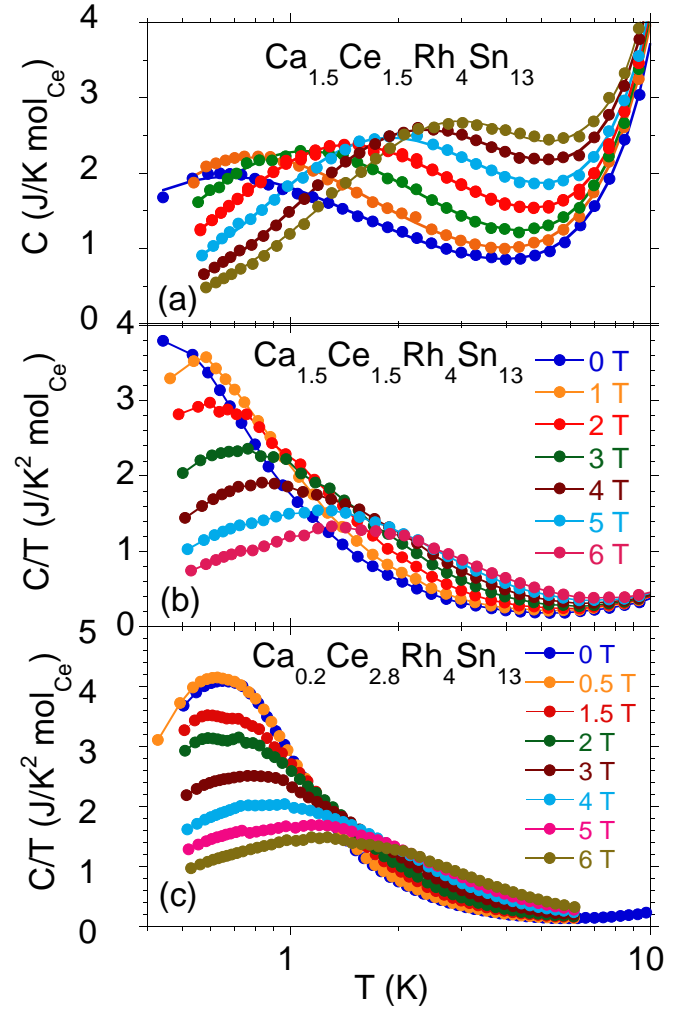


FIG. 19. (a) $C(T)$ vs T and (b) $C(T)/T$ vs T for $\text{Ca}_{1.5}\text{Ce}_{1.5}\text{Rh}_4\text{Sn}_{13}$. In panel (a) the lines represent the fit of the resonance level model to the experimental data. Panel (b) shows $C(T)/T$ at various magnetic fields for $\text{Ca}_{0.2}\text{Ce}_{2.8}\text{Rh}_4\text{Sn}_{13}$.

susceptibility χ and inverse susceptibility data, $1/\chi$, for $\text{Ca}_{1.5}\text{Ce}_{1.5}\text{Rh}_4\text{Sn}_{13}$, measured in a magnetic field of 500 Oe. The experimental $\chi(T)$ and $1/\chi(T)$ data can be well described in terms of CEF model⁶²:

$$\chi_{\text{CEF}} = \frac{N\mu_B^2}{k_B} \frac{\sum_i (\frac{a_i}{T} + b_i) e^{-\beta\Delta_i}}{\sum_i g_i e^{-\beta\Delta_i}} + \chi_0. \quad (5)$$

(Here, the summations run over all i states of energies E_i with $\Delta_i = E_i - E_0$ and Boltzman constant, k_B). This model appropriately reflects the tetragonal Ce point symmetry, where the $J = 5/2$ multiplet of the Ce^{3+} ion splits into three doublets which are separated from the ground state by energies $\Delta_1 \approx 26$ K and $\Delta_2 \approx 303$ K, respectively, and $\chi_0 \approx -0.0013$ emu/mol. The tetragonal symmetry of the CEF may indicate the structural deformation of the Sn_{12} cages in each of the $\text{Ca}_{1-x}\text{Ce}_x\text{Rh}_4\text{Sn}_{13}$ alloys. Recently³⁵, we documented that this subtle structural transition from the simple cu-

bic structure at room temperature to a superlattice variant near $T = 160$ K modifies the electronic structure and various physical properties of $RE_3M_4Sn_{13}$ compounds, where $RE = La$ or Ce and M is a d -electron-type metal. Indeed, for the compounds in the $Ca_{1-x}Ce_xRh_4Sn_{13}$ series with $x > 1$, the measurements of electrical resistivity reveal an abnormal change at $T_D \sim 160$ K, which could be interpreted as a transition between the semi-metallic ($T < T_D$) and metallic ($T > T_D$) state, generated by a distortion of Sn_{212} cage. This interpretation is very probable, with consideration that the structural distortion was also found in the parent compound $Ce_3Rh_4Sn_{13}$. In this case, the $Ca_{1-x}Ce_xRh_4Sn_{13}$ series appears to have a critical concentration $x_c \approx 1$, which separates the different behaviors of $Ca_3Rh_4Sn_{13}$ doped with Ce . The in-

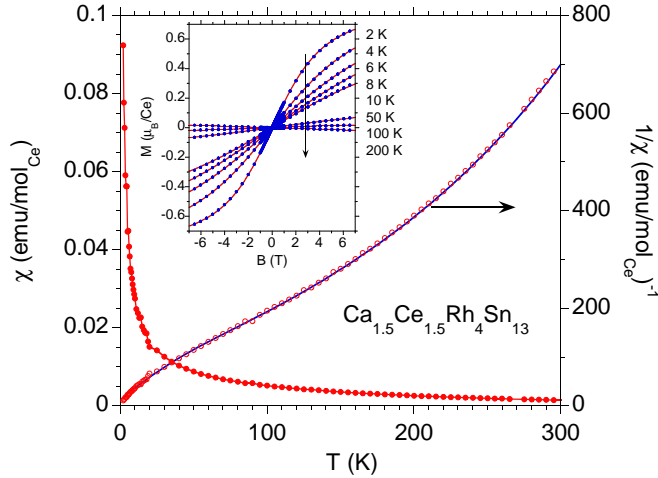


FIG. 20. Magnetic susceptibility χ and $1/\chi$ for $Ca_{1.5}Ce_{1.5}Rh_4Sn_{13}$ in an external field of 500 Oe. The blue line represents the CEF fit to the $1/\chi$ data, with the two excited doublets separated from the ground state doublet by energy $\Delta_1 = 26$ K and $\Delta_2 = 303$ K, respectively. Inset: Magnetization M vs B isotherms for $Ca_{1.5}Ce_{1.5}Rh_4Sn_{13}$ which are characteristic of paramagnets and well approximated by the Langevin function $L(\xi) = \coth(\xi) - 1/\xi$, where $\xi = \mu B/k_B T$ with a total magnetic moment $\mu \approx 0.9 \mu_B$ at $T = 1.8$ K.

set to Fig. 20 shows the magnetization M vs B isotherms for $Ca_{1.5}Ce_{1.5}Rh_4Sn_{13}$ which are characteristic of paramagnets. They are well approximated by the Langevin function $L(\xi) = \coth(\xi) - 1/\xi$, where $\xi = \mu B/k_B T$, with the total magnetic moment $\mu \approx 0.9 \mu_B$ at $T = 1.8$ K. The M vs B isotherms do not show any hysteresis in the field dependence of M and we noted that the magnetization M is well approximated by the Langevin function for all the components of the $Ca_{1-x}Ce_xRh_4Sn_{13}$ series with $x > 1$.

Finally, in Fig. 21 we present the electrical resistivity of $Ca_{1.5}Ce_{1.5}Rh_4Sn_{13}$ (a) and $Ca_{0.2}Ce_{2.8}Rh_4Sn_{13}$ (b) under applied external pressure. The pressure effect $\frac{d\rho}{dP}$ is strong and positive (in the upper panel the resistivity at $P = 1.29$ GPa for the sample $x = 1.5$ deviates from the expected value, this effect is not discussed here. The subtle DOS effect at ϵ_F could be a possible reason of this

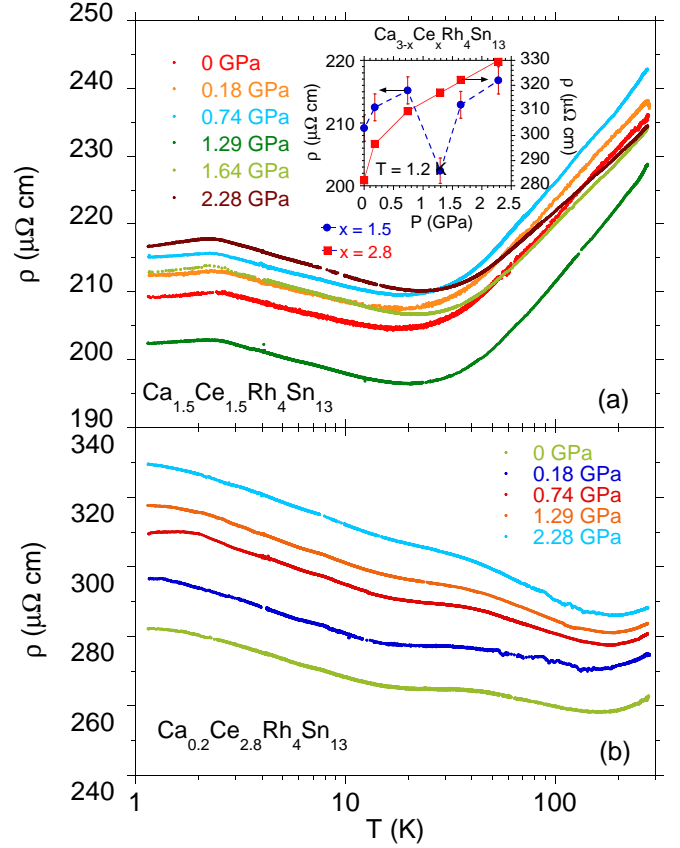


FIG. 21. Electrical resistivity for (a) $Ca_{1.5}Ce_{1.5}Rh_4Sn_{13}$ and (b) $Ca_{0.2}Ce_{2.8}Rh_4Sn_{13}$ under applied pressure. Inset: Electrical resistivity at $T = 1.2$ K as a function of P .

abnormal behavior, it seems to be also possible that this is not a physical effect). A similar $\frac{d\rho}{dP} > 0$ behavior was recently observed for $Ce_3Co_4Sn_{13}$ and $Ce_3Rh_4Sn_{13}$ ⁵⁶ below the temperature of structural distortion and has been documented as a result of the band-structure properties near the Fermi energy under applied pressure.

V. CONCLUSIONS

The resistivity of Ce -substituted $Ca_3Rh_4Sn_{13}$ samples exhibits *high-temperature* superconductivity with the highest $T_c \approx 8$ K for $Ca_{2.8}Ce_{0.2}Rh_4Sn_{13}$. This is much higher than the value of $T_c = 4.8$ K for the parent compound. Magnetic measurements as well as theoretical band structure calculations predict a nonmagnetic ground state in $Ca_3Rh_4Sn_{13}$. It is possible, however, that the substitution of Ce for Ca forms a spin-glass-like phase which coexists with the superconducting phase and that the superconductivity is enhanced in this magnetic state. Although attempts have been made to explain the increase in T_c for unconventional superconductors exhibiting disorder or a magnetic phase, there is no clear answer as to why T_c rises in materials in which a spin-glass-like state coexists with superconductivity. The basis for the

interpretation of the results presented here is that the Ce substitution into the superconducting parent compound $\text{Ca}_3\text{Rh}_4\text{Sn}_{13}$ increases the inhomogeneity and chemical pressure in the sample. It is also possible that the substitution affects T_c through the increase of the DOS at the Fermi level. But results of the LSDA calculations presented in Fig. 16 do not support such a scenario: the DOS at the Fermi level for $\text{Ce}_3\text{Rh}_4\text{Sn}_{13}$ is slightly smaller than for $\text{Ca}_3\text{Rh}_4\text{Sn}_{13}$, though it does not exclude the possibility that the DOS is larger at a lower doping level. It is also difficult to definitely say how the substitution modifies other parameters that enter the McMillan expression for T_c . The Ce-doping drives $\text{Ca}_3\text{Rh}_4\text{Sn}_{13}$ through a T_c vs x superconducting *dome* between $x = 0$ and $x \approx 1.2$, similar to that documented for high- T_c cuprates, and for $x > 1.2$, the compounds settle into a Kondo-lattice state with structural distortion. Taken together, the resistivity, specific heat and susceptibility measurements are suggestive of granular superconductivity, a form of inhomogeneous superconductivity. Interestingly, a *high* value of T_c was observed upon Ce substitution but in the absence of the structural deformation, while in the Kondo-lattice range, the slight structural deformation is visible in the resistivity data. Within the superconducting *dome* region we documented, the relationship between the electronic

structure and the resistivity under external pressure for $T > T_c$. Namely, we calculated a linear decrease of the DOS at E_F with P which correlates well with the measured negative coefficient $\frac{d\rho}{dP}$. These observations raise questions regarding the sensitivity of Cooper pairing in $\text{Ca}_{3-x}\text{Ce}_x\text{Rh}_4\text{Sn}_{13}$ and similar skutterudite-related systems to the electronic structure, atomic disorder and bonding, which suggests further detailed investigation.

VI. ACKNOWLEDGMENTS

The research was supported by National Science Centre (NCN) on the basis of Decision No. DEC-2012/07/B/ST3/03027. M.M.M. acknowledges support by NCN under grant DEC-2013/11/B/ST3/00824. P.W. acknowledges support by NCN under grant DEC-2015/17/N/ST3/02361. High-pressure research at the University of California, San Diego, was supported by the National Nuclear Security Administration under the Stewardship Science Academic Alliance program through the U. S. Department of Energy under Grant Number DE-NA0001841. One of us (A.Ś.) is grateful for the hospitality at the University of California, San Diego (UCSD).

-
- ¹ S. Zapf, H. S. Jeevan, T. Ivek, F. Phister, F. Klingert, S. Jiang, D. Wu, P. Gegenwart, R. K. Kremer, and M. Dressel, Phys. Rev. Lett. **110**, 237002 (2013).
- ² K. Nadeem, W. Zhang, D. Y. Chen, Z. A. Ren, and X. G. Qiu, Sci. Rep. **5**, 10700 (2015); doi:10.1038/srep10700
- ³ M. B. Maple, P.-C. Ho, V. S. Zapf, N. A. Frederick, E. D. Bauer, W. M. Yuhasz, F. M. Woodward and J. W. Lynn, J. Phys. Soc. Jpn. Suppl. **71**, 23 (2002)
- ⁴ R. Vollmer, A. Fait, C. Pfleiderer, H. v. Löhneysen, E. D. Bauer, P.-C. Ho, V. Zapf, and M. B. Maple, Phys. Rev. Lett. **90**, 057001 (2003).
- ⁵ J. S. Kim, D. J. Mixson, D. J. Burnette, T. Jones, P. Kumar, B. Andraka, G. R. Stewart, V. Craciun, W. Acree, H. Q. Yuan, D. Vandervelde, and M. B. Salamon, Phys. Rev. B **71**, 212505 (2005)
- ⁶ T. Takeuchi, T. Yasuda, M. Tsujino, H. Shishido, R. Settai, H. Harima, and Y. Onuki, J. Phys. Soc. Jpn. **76** 014702 (2007).
- ⁷ A. Bianchi, R. Movshovich, M. Jaime, J. D. Thompson, P. G. Pagliuso, and J. L. Sarrao, Phys. Rev. B **64**, 220504(R) (2001).
- ⁸ A. Ślebarski, M. Fijałkowski, M. M. Maška, M. Mierzejewski, B. D. White, and M. B. Maple, Phys. Rev. B **89**, 125111 (2014).
- ⁹ A. Ślebarski, M. M. Maška, M. Fijałkowski, C. A. McElroy, and M. B. Maple, J. Alloys Compds. **646**, 866 (2015).
- ¹⁰ H. Xiao, T. Hu, A. P. Dioguardi, N. apRoberts-Warren, A. C. Shockley, J. Crocker, D. M. Nisson, Z. Viskadourakis, X. Tee, I. Radulov, C. C. Almasan, N. J. Curro, and C. Panagopoulos, Phys. Rev. B **85**, 024530 (2012).
- ¹¹ A. P. Dioguardi, J. Crockeoberris-Warren, P. C. Confield, S. L. Bud'ko, S. Ran, and N. J. Curro, Phys. Rev. Lett. **111**, 207201 (2013).
- ¹² J. P. Remeika, G.P. Espinosa, A. S. Cooper, H. Barz, J.M. Rowel, D. B. McWhan, J. M. Vandenberg, D. E. Moncton, Z. Fizek, L. D. Woolf, H. C. Hamaker, M. B. Maple, G. Shirane, and W. Thomlinson, Sol. State Commun. **34**, 923 (1980); J. L. Hodeau, M. Marezio, J. P. Remeika, and C. H. Chen, *ibid.* **42**, 97 (1982).
- ¹³ J. Rodriguez-Carvajal, Physica B **192**, 55 (1993).
- ¹⁴ L. E. Klintberg, S. K. Goh, P. L. Alireza, P. J. Saines, D. A. Tompsett, P. W. Logg, J. Yang, B. Chen, K. Yoshimura, and F. M. Grosche, Phys. Rev. Lett. **109**, 237008 (2012).
- ¹⁵ S. K. Goh, D. A. Tompsett, P. J. Saines, H. C. Hang, T. Matsumoto, M. Imai, K. Yoshimura, and F. M. Grosche, Phys. Rev. Lett. **114**, 097002 (2015).
- ¹⁶ A. Ślebarski and J. Goraus, Phys. Rev. B **88**, 155122 (2013).
- ¹⁷ J. P. A. Westerveld, D. M. R. Lo Cascio, and H. Bakker, J. Phys. F: Met. Phys. **17**, 1963 (1987).
- ¹⁸ J. P. A. Westerveld, D. M. R. Lo Cascio, H. Bakker, B. O. Loopstra, and K. Goubitz, J. Phys.: Condens. Matter. **1**, 5689 (1989).
- ¹⁹ A. Ślebarski, B. D. White, M. Fijałkowski, J. Goraus, J. J. Hamlin, and M. B. Maple, Phys. Rev. B **86**, 205113 (2012).
- ²⁰ K. Koepernik, H. Eschrig, Phys. Rev. B **59**, 1743 (1999); I. Opahle, K. Koepernik, H. Eschrig, Phys. Rev. B **60**, 14035 (1999); K. Koepernik, B. Velicky, R. Hayn, H. Eschrig, Phys. Rev. B **55**, 5717 (1997); H. Eschrig, K. Koepernik, I. Chaplygin, J. Solid State Chem. **176**, 482 (2003); www.fplo.de
- ²¹ Elk FP-LAPW code, version 3.1.12, <http://elk.sourceforge.net/>

- 22 J.P. Perdew, Y. Wang, Phys. Rev. B **45**, 13244 (1992).
- 23 C. V. Tomy, G. Balakrishnan, and D. McK. Paul, Phys. Rev. B **56**, 8346 (1997).
- 24 A. Ślebarski, P. Witas, J. Goraus, L. Kalinowski, and M. Fijałkowski, Phys. Rev. B **90**, 075123 (2014).
- 25 H. F. Liu, C. N. Kuo, C. S. Lue, K. -Z. Syu, and Y. K. Kuo, Phys. Rev. B **88**, 115113 (2013).
- 26 A. F. Fang, X. B. Wang, P. Zheng, and N. L. Wang, Phys. Rev. B **90**, 035115 (2014).
- 27 D. Moseley, K. A. Yates, W. R. Branford, A. S. Sefat, D. Mandrus, S. J. Stuard, S. Salem-Sugui, L. Ghivelder, and L. F. Cohen, Europhys. Lett. **111**, 37005 (2015).
- 28 J. Yang, B. Chen, C. Michioka, and K. Yoshimura, J. Phys. Soc. Jpn. **79**, 113705 (2010).
- 29 K. Wang and C. Petrovic, Phys. Rev. B **86**, 024522 (2012).
- 30 S. Gerber, J. L. Gavilano, M. Medarde, V. Pomjakushin, C. Baines, E. Pomjakushina, K. Conder, and M. Kenzelmann, Phys. Rev. B **88**, 104505 (2013).
- 31 A. Haas, D. Wichert, G. Bruls, B. Lüthi, G. Balakrishnan, and D. McK. Paul, J. Low Temp. Phys. **114**, 285 (1999).
- 32 We did not find structural distortion for $\text{Ca}_3\text{Rh}_4\text{Sn}_{13}$. Considering a similar situation for $\text{Ca}_{2.8}\text{Ce}_{0.2}\text{Rh}_4\text{Sn}_{13}$, it can be assumed that the crystal field ground state of Ce ion in the cubic symmetry is a doublet.
- 33 A. Ślebarski, M. Fijałkowski, and J. Goraus, Intermetallics **54**, 199 (2014).
- 34 K. D. Schotte and U. Schotte, Phys. Lett. **55**, 38 (1975).
- 35 A. Ślebarski and J. Goraus, Phys. Rev. B **88**, 155122 (2013).
- 36 A. Gerber, T. Grenet, M. Cyrot, and J. Beille, Phys. Rev. Lett. **65**, 3201 (1990); R. Gross, P. Chaudhari, D. Dimos, A. Gupta, and G. Koren, Phys. Rev. Lett. **64**, 228 (1990); A. Gerber, T. Grenet, M. Cyrot, and J. Beille, Phys. Rev. B **43**, 12935 (1991); J. J. Neumeier and M. B. Maple, Phys. C **191**, 158 (1992); E. A. Early, C. C. Almasan, R. F. Jardim, and M. B. Maple, Phys. Rev. B **47**, 433 (1993); R. F. Jardim, L. Ben-Dor, D. Stroud, and M. B. Maple, Phys. Rev. B **50**, 10080 (1994); D. G. Stell, J. D. Hettinger, F. Yuan, D. J. Miller, K. E. Gray, J. H. Kang and J. Tavacchio, Appl. Phys. Lett. **68**, 120 (1996).
- 37 K. Nakatsuji, A. Sumiyama, Y. Oda, T. Yasuda, R. Settai, and Y. Onuki, J. Phys. Soc. Jpn. **75**, 084717 (2006).
- 38 V. V. Schmidt, *The Physics of Superconductors*, ed. P. Müllerand and A. V. Ustinov (Berlin: Springer, 1977).
- 39 M.-A. Méasson, D. Braithwaite, J. Flouquet, G. Seyfarth, J. P. Brison, E. Lhotel, C. Paulsen, H. Sugawara, and H. Sato, Phys. Rev. B **70**, 064516 (2004).
- 40 M.-A. Méasson, D. Braithwaite, G. Lapertot, J.-P. Brison, J. Flouquet, P. Bordet, H. Sugawara, and P. C. Canfield, Phys. Rev. B **77**, 134517 (2008).
- 41 S. L. Budko and P. C. Canfield, Phys. Rev. B **65**, 212501 (2002).
- 42 S. V. Shulga, S.-L. Drechsler, G. Fuchs, K.-H. Müller, K. Winzer, M. Heinecke, and K. Krug, Phys. Rev. Lett. **80**, 1730 (1998).
- 43 Yoichi Ando, G. S. Boebinger, A. Passner, L. F. Schneemeyer, T. Kimura, M. Okuya, S. Watauchi, J. Shimoyama, K. Kishio, K. Tamasaku, N. Ichikawa, and S. Uchida, Phys. Rev. B **60**, 12475 (1999).
- 44 G. M. Eliashberg, Sov. Phys. JEPT **11** (1960) 696; **12** (1961) 1000.
- 45 W. L. McMillan, Phys. Rev. **167**, 331 (1968).
- 46 R. C. Dynes, Sol. State Commun. **10** 615 (1972).
- 47 J. J. Hopfield, Phys. Rev. **186**, 443 (1969).
- 48 Y. Shao and X. Zhang, J. Phys.: Condens. Matter **16** 1103 (2004).
- 49 F. D. Murnaghan, Proc. Natl. Acad. Sci. USA **30**, 244 (1944); F. Birch, Phys. Rev. **71**, 809 (1947).
- 50 J. Bardeen, L. N. Cooper, and J. R. Schrieffer, Phys. Rev. **108**, 1175 (1957).
- 51 P. E. Seiden, Phys. Rev. **179**, 458 (1969).
- 52 A. I. Larkin, V. I. Mel'nikov, and D. E. Khomelnitskii, Zh. Eksp. Teor. Fiz. **60**, 846 (1971) [Sov. Phys. JETP **33**, 458 (1971)].
- 53 V. M. Galitski and A. I. Larkin, Phys. Rev. B **66**, 064526 (2002).
- 54 B. A. Young, T. Saab, B. Cabrera, J. J. Cross, R. M. Clarke, and R. A. Abusaidi, J. Appl. Phys. **86**, 6975 (1999).
- 55 E. Z. Kuchinskii, N. A. Kuleeva, and M. V. Sadovskii, J. Exp. Theoret. Phys. **120**, 1055 (2015); J. Mayoh and A. M. Garca-Garca, Phys. Rev. B **92**, 174526 (2015); I. S. Burmistrov, I. V. Gornyi, and A. D. Mirlin, Phys. Rev. Lett. **108**, 017002 (2012); Luca Dell'Anna, Phys. Rev. B **88**, 195139 (2013); I. Martin, D. Podolsky, and S. A. Kivelson Phys. Rev. B **72**, 060502(R) (2005); S. Chakraborty, D. Snychal, and A.-M. S. Tremblay, Phys. Rev. B **84**, 054545 (2011); M. M. Maška, Ž. Šledz, K. Czajka, and M. Mierzejewski, Phys. Rev. Lett. **99**, 147006 (2007); P. M. Smith and M. P. Kennett, Phys. Rev. B **88**, 214518 (2013).
- 56 A. Ślebarski and J. Goraus, and P. Witas, Phys. Rev. B **92**, 155136 (2015).
- 57 P. Hohenberg and W. Kohn, Phys. Rev. **136**, B864 (1964).
- 58 O. Gunnarsson and K. Schönhammer, Phys. Rev. B **28**, 4315 (1983).
- 59 J. C. Fuggle, F. U. Hillebrecht, Z. Zolnieriek, R. Lässer, Ch. Freiburg, O. Gunnarsson, and K. Schönhammer, Phys. Rev. B **27**, 7330 (1983).
- 60 A. Ślebarski, M. Radłowska, T. Zawada, M. B. Maple M, A. Jezierski, and A. Zygmunt Phys. Rev. B **66**, 104434 (2002); A. Ślebarski, T. Zawada, J. Spalek, and A. Jezierski, Phys. Rev. B **70**, 235112 (2004).
- 61 The occupation number of the $4f$ shell, $n_f = 1 - \nu$, and $\nu \cong \frac{I(f^0)}{I(f^0)+I(f^1)+I(f^2)}$. In case of the $\text{Ca}_{3-x}\text{Ce}_x\text{Rh}_4\text{Sn}_{13}$ series, the $3d^9 4f^0$ line is not observed in the Ce $3d$ XPS spectra, this suggests a stable configuration Ce^{3+} of the $4f$ shell.
- 62 J. Mulak, J. Less Common Metals, **121**, 141 (1986).